IEEE Sensors Council

UWB-IMU-Odometer Fusion Localization Scheme: Observability Analysis and Experiments

Boli Zhou, Hongbin Fang, *Member, IEEE*, and Jian Xu

***Abstract*—In this article, we present a novel ultrawideband (UWB)-inertial measurement unit (IMU)-odometer fusion localization scheme for nonholonomic ground robots in global positioning system (GPS)-denied environments. To overcome the severe drift problems caused by the large acceleration bias of low-cost IMUs, rather than using the conventional IMU-only propagation model, a wheel odometer and a three-axis gyroscope are integrated to propagate the system states. Furthermore, the observability conditions of the proposed system with nonholonomic constraints are theoretically derived by a nonlinear observability analysis. The results reveal the minimum number of anchors (or leader robots) required for position observability (at least three anchors for UWB-time of arrival (ToA) measurements and one anchor for both ToA and angle-of-arrival (AOA) measurements). In addition, the system inputs (linear velocity and angular velocity along different axes) need to be excited for attitude observability. Simulations and experiments have verified that the proposed approach produces accurate position estimation and outperforms previous methods. Meanwhile, the position and attitude observability conditions have been verified through rich experiments, and the degenerated cases where the states cannot be observed are enumerated and tested, making the scheme complete.**

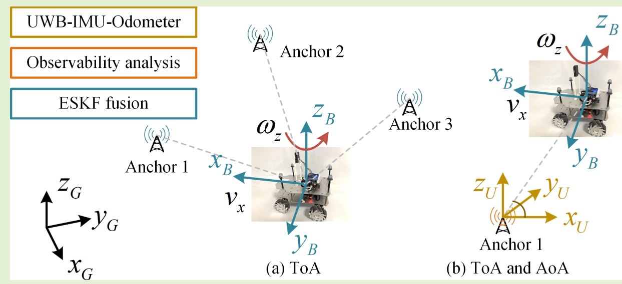

***Index Terms*—Error state Kalman filter (ESKF), nonholonomic constraints, observability analysis, sensor fusion, ultrawideband (UWB).**

I. Introduction

ACCURATE estimation of each robot's pose in a common frame is crucial for robot applications, such as collision avoidance and navigation. Conventional positioning techniques tend to rely on the aid of the global positioning system (GPS) outdoors or Wi-Fi positioning systems and RFID-based localization systems indoors. Although these techniques have already been widely adopted, they all have obvious limitations: the GPS provides meter-level accuracy outdoors and is commonly integrated with inertial navigation system (INS) [1], but it fails to work indoors due to sporadic access to satellite signals. Meanwhile, although the general Wi-Fi-based [2] or RFID-based indoor positioning systems [3] are easy to establish and deploy, the positioning accuracy is low. Therefore, obtaining accurate poses with bounded errors in GPS-denied environments is a practical problem that must be addressed. A prevalent solution is a simultaneous localization and mapping (SLAM) technology, which leverages onboard sensors, such as light detection and ranging (LiDAR) or cameras, for scene understanding and pose determination. Nonetheless, in these circumstances, high processing capabilities, high memory capacity, and advanced sensing systems are required. In addition, long-term drift errors and weak robustness to harsh environments remain difficult to handle. Compared with these localization schemes, ultrawideband (UWB) technology can provide centimeter-level ranging accuracy, with the advantages of low power consumption, high-bandwidth communication, and strong robustness, making it a priority for building indoor communication and positioning networks.

Typical research and applications of UWB-only-based robot localization systems generally use trilateration approaches [4] that rely on multiple fixed anchors to determine the robot's position. In addition, integrating UWB with inertial measurement unit (IMU) is a popular and robust solution to estimate both the position and the attitude. You et al. [5] proposed an unscented Kalman filter (UKF)-

Manuscript received 4 November 2022; revised 7 December 2022; accepted 7 December 2022. Date of publication 22 December 2022; date of current version 31 January 2023. This work was supported in part by the National Key Research and Development Program of China under Grant 2020YFB1312900, in part by the Joint Fund of Ministry of Education for Equipment Pre-Research under Grant 8091B032150, and in part by the National Natural Science Foundation of China under Grant 11932015. The associate editor coordinating the review of this article and approving it for publication was Prof. Yulong Huang. *(Corresponding author: Hongbin Fang.)*

The authors are with the Institute of AI and Robotics, the MOE Engineering Research Center of AI and Robotics, and the Shanghai Engineering Research Center of AI and Robotics, Fudan University, Shanghai 200433, China (e-mail: blzhou20@fudan.edu.cn; fanghongbin@fudan.edu.cn; jian_xu@fudan.edu.cn).

Digital Object Identifier 10.1109/JSEN.2022.3228296

based pose estimation approach for quadrotor UAVs, which is suitable for nonlinear observations and effectively improves the estimation accuracy of UWB-IMU nonlinear systems. Li et al. [6] used the extended Kalman filter (EKF) to fuse UWB and IMU measurements to estimate the position and velocity of UAVs as well as the acceleration and angular velocity biases. In addition, Goudar and Schoellig [7] proposed a tightly coupled UWB-aided inertial localization scheme with online spatial–temporal calibration for UAV systems, which reduces the positioning errors caused by time delay and extrinsic parameters between sensors. In these algorithm frameworks, state propagation is performed by integrating the acceleration and angular velocity of the IMU, and the operating platforms are typically UAV systems with frequent sharp motions. However, for ground robots with gentle or even uniform motions, the actual acceleration and angular velocity are usually tiny or even close to zero, which makes it difficult for a low-cost IMU to detect the motion. Not only that the measurement noise and biases of low-cost IMUs, especially from acceleration, will lead to huge drift errors and fluctuations. Therefore, high-precision IMUs are often required for wheeled robot positioning in the UWB-IMU fusion. Li et al. [8] proposed an accurate 6-DOF positioning algorithm for underground coal mine robots, where the error state Kalman filter (ESKF) was used to fuse UWB and high-precision IMU measurements, with a positioning accuracy close to that of the advanced LiDAR odometry. In addition to methods to improve the accuracy of IMU itself, velocity observation is also an effective way to constrain drifts. Cao et al. [9] proposed a speed estimator that solves the velocity drift problem in low-cost IMU and UWB fusion by continuously monitoring UWB range variations instead of integrating the acceleration data. This method can obtain accurate 2-D pose estimation for a low-cost IMU-based wheeled robot; however, it is performed under the assumption that the robot is moving at a constant speed. Wang and Li [10] proposed a pedestrian positioning method by fusing UWB and IMU data based on particle filtering, in which the zero-velocity update (ZUPT) method was used to detect the zero-velocity state and constrain the cumulative errors. Brossard et al. [11] achieved accurate pure inertial navigation of a car under long-range trajectories by detecting the zero-speed state of the IMU through a recurrent neural network combined with the ZUPT method. What these methods have in common is that they are all effective in estimating or detecting the velocity. Note that using a wheel odometer is the most direct and effective way to observe the velocity and bound the drift of a ground robot with no need to design a speed estimator or employ the ZUPT method. Therefore, to make the low-cost IMU positioning scheme feasible, noisy acceleration measurements are excluded, and one-axis linear velocity from the wheel odometer and three-axis angular velocities from the gyroscope are combined to propagate the 3-D motion.

In addition, observability is a necessary condition for the convergence of state variables to unbiased estimates of the true system states [12]. To study the observability, the commonly used methods include a linear matrix rank test for linear systems and a differential geometry approach that is preferable for nonlinear systems. Previous studies have examined the observability properties of multisensor fusion systems, such as camera-IMU systems [12], UWB-IMU systems [13], and GPS-IMU systems [14]. In particular, the observability of UWB in combination with inertial sensors or wheel odometers has attracted significant attention. Goudar and Schoellig [7] conducted an observability analysis of a tightly coupled UWB-IMU system with extrinsic parameters. The object of this study is a moving target, such as a human or a drone, which can move and rotate along all three axes of the body, rather than a general ground robot with nonholonomic constraints, which often cannot move purely laterally or upward perpendicular to the ground. Therefore, sufficient motion excitation can be provided for the IMU-only propagation model with acceleration and angular velocity as system inputs in [7]. In general, different models (e.g., different system inputs) will lead to different observability results. Araki et al. [15] investigated the observability of relative poses between multiple robots equipped with UWB and wheel odometers, where only 2-D models were considered, and absolute poses were not included in the states. Absolute information, such as anchors, is beneficial in making absolute poses observable [16]. Fontanelli et al. [17] showed that in 2-D space, when two UWB anchors are used and the robot does not move in a straight line, the system is globally observable. However, the characteristics of wheel odometers indicate that the motion model is 2-D, so UWB anchors generally need to be arranged in the same horizontal plane as the robots.

In this article, the object of our analysis is the ground robots with nonholonomic constraints. Since the IMU-odometer motion model used is a 3-D model with nonholonomic constraints, we investigate the observability of the UWB-IMU-odometer (UIO) system based on this 3-D model. In addition, the observability of the absolute poses is analyzed since the absolute information is known and used, such as the positions of the anchors or the poses of moving leader robots (LRs). Here, LRs refer to robots that can obtain accurate global poses and play the role of anchors. The main objective of this study is to propose a novel approach based on UIO fusion for resource-constrained ground robots. Meanwhile, observability analyses are carried out to deepen the insight into the proposed UIO system. The specific contributions achieved in this study are given as follows.

1) A novel multisensor fusion localization scheme combining UWB, wheel odometers, and IMUs is proposed to achieve accurate global localization and avoid drifts and fluctuation caused by integrating low-grade accelerometer data.
2) The observability conditions for the proposed UIO-fusion system are derived theoretically, which suggests that at least three noncollinear anchors are required to make the robot's position observable. In addition, the linear velocity along the body x-axis and the angular velocity along the body z-axis are excited to ensure the attitude observability. Special cases in which the states are unobservable are enumerated.
3) UWB-angle-of-arrival (AOA) protocol is incorporated into the system, and the observability conditions for position and attitude are derived from theoretical analyses; the incorporation of AoA reduces the observ-

ability conditions, allowing robot localization with only one anchor.

4) Through both simulations and experiments, the effectiveness and superiority of the proposed scheme over the conventional techniques are demonstrated and validated. The derived observability conditions are fully verified by simulations and practical tests.

II. Problem Statement

Traditional UWB-IMU fusion [5], [6], [8], [9], [10], [13] techniques face the following problems: 1) the large drifts associated with the fusion of low-cost IMU and UWB and 2) the observability of the UIO system has not yet been analyzed. This research addresses these challenges separately. First, a wheel odometer is used to avoid imprecise velocity estimation, enabling accurate pose estimation based on low-grade IMUs. Compared to the conventional INS formulated in [18], acceleration data from the IMUs are excluded, and only the readings from the gyroscopes and wheel encoders are utilized to quantify the 3-D motion. Second, observability analyses based on a differential geometry approach [19] are carried out to deepen the insight into the proposed system with different measurement models (time of arrival (ToA)/both ToA and AoA). Meanwhile, a geometric interpretation of observability is provided. The advantages of the proposed method and the observability theorems of the system are verified by rich experiments, in which each ground robot runs a separate state estimator based on the ESKF by fusing wheel odometer, IMU, and UWB data.

III. Models

In this section, the notations are first explained; then, the system states to be estimated are presented; and the sensor measurements, including the wheel odometer, the gyroscope, and the UWB, are modeled.

A. Notations

Without loss of generality, an "LR" is used to act as a static or a moving anchor, and its absolute information is known. The other robots are called "follower robots" (FRs). We consider a team of N robots $\{\mathrm{R}_N\}$, consisting of N_l LRs $\{\mathrm{LR}_{N_l}\}$ and N_f FRs $\{\mathrm{FR}_{N_f}\}$. The global frame and body frame of the robot are denoted by $\{\mathcal{G}\}$ and $\{\mathcal{B}\}$, respectively. For convenience, the frame $\{\mathcal{B}\}$ coincides with the IMU frame, with the origin at the robot center, the x-axis pointing in the forward direction of the robot, and the z-axis pointing upward.

For two arbitrary frames $\{\mathcal{U}\}$ and $\{\mathcal{V}\}$, we adopt ${}^{U}_{V}\mathbf{p}$ and ${}^{U}_{V}\mathbf{q}$ to, respectively, describe the position and quaternion orientation of the frame $\{\mathcal{V}\}$ with respect to the frame $\{\mathcal{U}\}$. ${}^{U}_{V}\mathbf{R}$ is the corresponding rotation matrix of ${}^{U}_{V}\mathbf{q}$. For an arbitrary variable a, we use a_t, a_m, $\hat{a}$, and $\tilde{a}$ to, respectively, denote the true, measured, estimated, and error value of a. Furthermore, the following two operators are defined:

$$\boldsymbol{\Omega}(\boldsymbol{\omega}) = \begin{bmatrix} 0 & -\boldsymbol{\omega}^{\mathrm{T}} \\ \boldsymbol{\omega} & -\lfloor\boldsymbol{\omega}\rfloor_\times \end{bmatrix}, \quad [\mathbf{q}]_l = q_w\mathbf{I} + \begin{bmatrix} 0 & -\mathbf{q}_v^{\mathrm{T}} \\ \mathbf{q}_v & \lfloor\mathbf{q}_v\rfloor_\times \end{bmatrix} \quad (1)$$

where $\mathbf{q} = [q_w\ \mathbf{q}_v^{\mathrm{T}}]^{\mathrm{T}}$ is a Hamilton quaternion and $[\cdot]_l$ is the left-quaternion-product matrix operator. For an arbitrary 3-D vector $\boldsymbol{\omega}$, $\lfloor\cdot\rfloor_\times$ is a skew-symmetric operator

$$\lfloor\boldsymbol{\omega}\rfloor_\times = \begin{bmatrix} 0 & -\omega_z & \omega_y \\ \omega_z & 0 & -\omega_x \\ -\omega_y & \omega_x & 0 \end{bmatrix}, \quad \boldsymbol{\omega} = \begin{bmatrix} \omega_x \\ \omega_y \\ \omega_z \end{bmatrix}. \quad (2)$$

B. UIO System

1) Propagation Model: A UIO system is specifically designed for one FR equipped with the wheel odometer. Excluding accelerometer data from a low-cost IMU, the three-axis gyroscope and the one-axis odometer constitute a reduced inertial-odometer system, with state variables parameterized by

$$\mathbf{x}(t) = \left[{}^{G}_{B}\mathbf{p}^{\mathrm{T}}(t), {}^{G}_{B}\mathbf{q}^{\mathrm{T}}(t), \mathbf{b}_g^{\mathrm{T}}(t)\right]^{\mathrm{T}} \in \mathbb{R}^{10} \quad (3)$$

where $\mathbf{b}_g$ is the time-varying gyroscope bias. For the sake of brevity, time t is omitted in the following. Measurements of the gyroscope $\mathbf{w}_m$ and the odometer $\mathbf{v}_m$ are modeled as

$$\mathbf{w}_m = \mathbf{w}_t + \mathbf{b}_g + \mathbf{n}_g, \quad \mathbf{v}_m = \mathbf{v}_t + \mathbf{n}_v \quad (4)$$

where $\mathbf{n}_v$ and $\mathbf{n}_g$ are zero-mean white Gaussian noises [18], [20]. Furthermore, after modifications to the pure IMU propagation model [18], the system dynamics are modeled as

$$\begin{aligned} {}^{G}_{B}\dot{\mathbf{p}} &= {}^{G}_{B}\mathbf{R}\left(\mathbf{v}_m - \mathbf{n}_v\right) \\ {}^{G}_{B}\dot{\mathbf{q}} &= \frac{1}{2}\boldsymbol{\Omega}\left(\mathbf{w}_m - \mathbf{b}_g - \mathbf{n}_g\right){}^{G}_{B}\mathbf{q} \\ \dot{\mathbf{b}}_g &= \mathbf{n}_{wg} \end{aligned} \quad (5)$$

where $\mathbf{n}_{wg}$ is the zero-mean white Gaussian noise, i.e., the gyro bias is modeled as a random walk process. In this article, we focus on generic nonholonomic ground robots, and thus, the body linear velocity and the noise yield

$$\mathbf{v}_t = [v_x, 0, 0]^{\mathrm{T}}, \quad \mathbf{n}_v = [n_{xv}, 0, 0]^{\mathrm{T}}. \quad (6)$$

2) Measurement Model With ToA: A UWB-distance measurement between an FR and LR_i is

$$d = \|{}^{G}_{L_i}\mathbf{p} - {}^{G}_{B}\mathbf{p}\|_2 + n_{di}, \quad i = 1, \ldots, s \quad (7)$$

where ${}^{G}_{L_i}\mathbf{p}$ represents the position of the ith LR in the global frame, which is known by FRs via communication. The measurement error n_{di} is assumed to be zero-mean Gaussian noise, $||\cdot||_2$ represents the Euclidean norm, and s denotes the number of LRs that are in the measurement range of the FR.

3) Measurement Model With Both ToA and AoA: AoA can be measured by calculating the phase difference of arrival through the UWB antenna array. Combined with the ToA protocol, distance, elevation, and azimuth angle can be measured by state-of-the-art hardware [21]. Furthermore, the position of the FR in the body frame of the LR (i.e., ${}^{L_i}_{B}\mathbf{p}$) can be obtained. The measurement model is

$${}^{L_i}_{B}\mathbf{p} = {}^{L_i}_{G}\mathbf{R}\left({}^{G}_{B}\mathbf{p} - {}^{G}_{L_i}\mathbf{p}\right) + \mathbf{n}_{ai}, \quad i = 1, \ldots, s \quad (8)$$

where $\mathbf{n}_{ai}$ are assumed to be the Gaussian noise [22].

IV. System With ToA Model

A. Observability Analysis

Observability is a necessary condition for the convergence of state variables, based on filter methods, to unbiased estimates of the true system states. In this study, we adopt a differential geometry approach [19], which is preferred for nonlinear systems, to derive the conditions under which the system is locally weakly observable.

Specifically, we treat the state space as a smooth manifold, which is a linear function of control input vectors. It is noted that the system is aimed at the ground robots with nonholonomic constraints, and only the forward velocity v_x from the wheel odometer and the 3-D angular velocity $\mathbf{w}_m$ from IMU are used as inputs. Since the noises do not affect the observability [7], [12], the Gaussian noise is removed from the system dynamics, and (5) is rearranged as a control affine form

$$\dot{\mathbf{x}} = \underbrace{\begin{bmatrix} \mathbf{0}_{3\times1} \\ -\frac{1}{2}\Xi\left({}^G_B\mathbf{q}\right)\mathbf{b}_g \\ \mathbf{0}_{3\times1} \end{bmatrix}}_{\mathbf{f}_0} + \underbrace{\begin{bmatrix} {}^G_B\mathbf{R}_{[:,1]} \\ \mathbf{0}_{7\times1} \end{bmatrix}}_{\mathbf{f}_1} v_x + \underbrace{\begin{bmatrix} \mathbf{0}_{3\times3} \\ \frac{1}{2}\Xi\left({}^G_B\mathbf{q}\right) \\ \mathbf{0}_{3\times3} \end{bmatrix}}_{\mathbf{f}_2} \mathbf{w}_m \tag{9}$$

where $\Xi({}^G_B\mathbf{q}) = [{}^G_B\mathbf{q}]_{l[:,2:4]}$, with the subscript $[\cdot]_{[:,\,i:j]}$ denoting the ith to the jth columns of a matrix, $\mathbf{f}_0$ is the drift vector field, and $\mathbf{f}_k (k = 1, 2)$ defines a smooth vector field on the manifold. We consider measurements using three LRs. For ease of calculation, we use z_{di} to reexpress the distance measurement

$$\begin{aligned} z_{di} &= h_{di}(\mathbf{x}) = \frac{1}{2}\left\|{}^G_{L_i}\mathbf{p} - {}^G_B\mathbf{p}\right\|_2^2, \mathbf{h}_d^T(\mathbf{x}) \\ &= \left[h_{d1}(\mathbf{x}), h_{d2}(\mathbf{x}), h_{d3}(\mathbf{x})\right] \end{aligned} \tag{10}$$

where $\mathbf{h}_d(\mathbf{x})$ denotes the vector of measurement function.

According to the definition, the system is locally weakly observable if the observation matrix, stacked by gradients of Lie derivatives, has full rank [19]. First, the zeroth-order Lie derivative of $\mathbf{h}_d(\mathbf{x})$ is the measurement vector itself, i.e.,

$$L^0\mathbf{h}_d(\mathbf{x}) = \mathbf{h}_d(\mathbf{x}) \tag{11}$$

and the gradient yields

$$\nabla L^0\mathbf{h}_d = \left[\Delta\mathbf{p}^{\mathrm{T}},\ \mathbf{0}_{3\times7}\right], \quad \Delta\mathbf{p} = \left[\Delta\mathbf{p}_1, \Delta\mathbf{p}_2, \Delta\mathbf{p}_3\right] \tag{12}$$

where $\Delta\mathbf{p}_i \triangleq {}^G_B\mathbf{p} - {}^G_{L_i}\mathbf{p} (i = 1, 2, 3)$, and the subscript L_i denotes the ith LR's body frame. We set $\mathbf{e}_1 = [1, 0, 0]^{\mathrm{T}}$, $\mathbf{e}_2 = [0, 1, 0]^{\mathrm{T}}$, and $\mathbf{e}_3 = [0, 0, 1]^{\mathrm{T}}$. The first-order Lie derivatives of $\mathbf{h}_d$ about $\mathbf{f}_i$ are $L^1_{\mathbf{f}_i}\mathbf{h}_d(\mathbf{x}) = \nabla L^0\mathbf{h}_d \cdot \mathbf{f}_i (i = 0, 1, 2)$, and we have

$$L^1_{\mathbf{f}_0}\mathbf{h}_d(\mathbf{x}) = L^1_{\mathbf{f}_2}\mathbf{h}_d(\mathbf{x}) = \mathbf{0}_{3\times1}, \quad L^1_{\mathbf{f}_1}\mathbf{h}_d(\mathbf{x}) = \Delta\mathbf{p}^{\mathrm{T}}{}^G_B\mathbf{R}\mathbf{e}_1. \tag{13}$$

The nonzero gradients are

$$\nabla L^1_{\mathbf{f}_1}\mathbf{h}_d = \begin{bmatrix} \mathbf{e}_1^{\mathrm{T}}{}^G_B\mathbf{R}^{\mathrm{T}} & -2\mathbf{e}_1^{\mathrm{T}}\mathbf{F}_1^0 & \mathbf{0}_{1\times3} \\ \mathbf{e}_1^{\mathrm{T}}{}^G_B\mathbf{R}^{\mathrm{T}} & -2\mathbf{e}_1^{\mathrm{T}}\mathbf{F}_2^0 & \mathbf{0}_{1\times3} \\ \mathbf{e}_1^{\mathrm{T}}{}^G_B\mathbf{R}^{\mathrm{T}} & -2\mathbf{e}_1^{\mathrm{T}}\mathbf{F}_3^0 & \mathbf{0}_{1\times3} \end{bmatrix} \tag{14}$$

where $\mathbf{F}_i^0 \triangleq ([\mathbf{q}_{p_i}]_l\Xi({}^G_B\mathbf{q}))^{\mathrm{T}}$, $\mathbf{q}_{p_i} \triangleq [0, ({}^G_B\mathbf{p} - {}^G_{L_i}\mathbf{p})^{\mathrm{T}}]$.

Furthermore, calculating the second-order Lie derivative of $\mathbf{h}_d$ about $\mathbf{f}_i$ via $L^2_{\mathbf{f}_1\mathbf{f}_i}\mathbf{h}_d(\mathbf{x}) = \nabla L^1_{\mathbf{f}_1}\mathbf{h}_d \cdot \mathbf{f}_i (i = 0, 1, 2)$ yields

$$L^2_{\mathbf{f}_1\mathbf{f}_0}\mathbf{h}_d(\mathbf{x}) = \begin{bmatrix} \mathbf{e}_1^{\mathrm{T}}\mathbf{F}_1^0\Xi\left({}^G_B\mathbf{q}\right)\mathbf{b}_g \\ \mathbf{e}_1^{\mathrm{T}}\mathbf{F}_2^0\Xi\left({}^G_B\mathbf{q}\right)\mathbf{b}_g \\ \mathbf{e}_1^{\mathrm{T}}\mathbf{F}_3^0\Xi\left({}^G_B\mathbf{q}\right)\mathbf{b}_g \end{bmatrix} \tag{15}$$

$$L^2_{\mathbf{f}_1\mathbf{f}_1}\mathbf{h}_d(\mathbf{x}) = [1, \ldots, 1]^{\mathrm{T}} \tag{16}$$

$$L^2_{\mathbf{f}_1\mathbf{f}_2}\mathbf{h}_d(\mathbf{x}) = \begin{bmatrix} -\mathbf{e}_1^{\mathrm{T}}\mathbf{F}_1^0\Xi\left({}^G_B\mathbf{q}\right) \\ -\mathbf{e}_1^{\mathrm{T}}\mathbf{F}_2^0\Xi\left({}^G_B\mathbf{q}\right) \\ -\mathbf{e}_1^{\mathrm{T}}\mathbf{F}_3^0\Xi\left({}^G_B\mathbf{q}\right) \end{bmatrix}. \tag{17}$$

The nonzero gradients are

$$\nabla L^2_{\mathbf{f}_1\mathbf{f}_0}\mathbf{h}_d = \begin{bmatrix} \mathbf{e}_1^{\mathrm{T}}\mathbf{F}^1 & -2\mathbf{e}_1^{\mathrm{T}}\mathbf{F}_1^2 & \mathbf{e}_1^{\mathrm{T}}\mathbf{F}_1^3 \\ \mathbf{e}_1^{\mathrm{T}}\mathbf{F}^1 & -2\mathbf{e}_1^{\mathrm{T}}\mathbf{F}_2^2 & \mathbf{e}_1^{\mathrm{T}}\mathbf{F}_2^3 \\ \mathbf{e}_1^{\mathrm{T}}\mathbf{F}^1 & -2\mathbf{e}_1^{\mathrm{T}}\mathbf{F}_3^2 & \mathbf{e}_1^{\mathrm{T}}\mathbf{F}_3^3 \end{bmatrix} \tag{18}$$

$$\nabla L^2_{\mathbf{f}_1\mathbf{f}_2}\mathbf{h}_d = \begin{bmatrix} \mathbf{0}_{3\times3} & \mathbf{0}_{3\times4} & \mathbf{0}_{3\times3} \\ -\mathbf{e}_3^{\mathrm{T}}{}^G_B\mathbf{R}^{\mathrm{T}} & 2\mathbf{e}_3^{\mathrm{T}}\mathbf{F}_1^0 & \mathbf{0}_{1\times3} \\ -\mathbf{e}_3^{\mathrm{T}}{}^G_B\mathbf{R}^{\mathrm{T}} & 2\mathbf{e}_3^{\mathrm{T}}\mathbf{F}_2^0 & \mathbf{0}_{1\times3} \\ -\mathbf{e}_3^{\mathrm{T}}{}^G_B\mathbf{R}^{\mathrm{T}} & 2\mathbf{e}_3^{\mathrm{T}}\mathbf{F}_3^0 & \mathbf{0}_{1\times3} \\ \mathbf{e}_2^{\mathrm{T}}{}^G_B\mathbf{R}^{\mathrm{T}} & -2\mathbf{e}_2^{\mathrm{T}}\mathbf{F}_1^0 & \mathbf{0}_{1\times3} \\ \mathbf{e}_2^{\mathrm{T}}{}^G_B\mathbf{R}^{\mathrm{T}} & -2\mathbf{e}_2^{\mathrm{T}}\mathbf{F}_2^0 & \mathbf{0}_{1\times3} \\ \mathbf{e}_2^{\mathrm{T}}{}^G_B\mathbf{R}^{\mathrm{T}} & -2\mathbf{e}_2^{\mathrm{T}}\mathbf{F}_3^0 & \mathbf{0}_{1\times3} \end{bmatrix} \tag{19}$$

$$\begin{aligned} &\mathbf{F}^1 \triangleq \lfloor\mathbf{b}_g\rfloor_\times {}^G_B\mathbf{R}^{\mathrm{T}}, \quad \mathbf{F}_i^3 \triangleq -\left\lfloor{}^G_B\mathbf{R}^{\mathrm{T}}\Delta\mathbf{p}_i\right\rfloor_\times \\ &\mathbf{F}_i^2 \triangleq \lfloor\mathbf{b}_g\rfloor_\times\left(\left[\mathbf{q}_{p_i}\right]_l\Xi\left({}^G_B\mathbf{q}\right)\right)^{\mathrm{T}}. \end{aligned} \tag{20}$$

Finally, the third-order Lie derivative of $\mathbf{h}_d$ with respect to $\mathbf{f}_0$ and the corresponding gradient are computed as follows:

$$L^3_{\mathbf{f}_1\mathbf{f}_0\mathbf{f}_0}\mathbf{h}_{di}(\mathbf{x}) = \nabla L^2_{\mathbf{f}_1\mathbf{f}_0}\mathbf{h}_d \cdot \mathbf{f}_0 = \begin{bmatrix} \mathbf{e}_1^{\mathrm{T}}\mathbf{F}_1^2\Xi\left({}^G_B\mathbf{q}\right)\mathbf{b}_g \\ \mathbf{e}_1^{\mathrm{T}}\mathbf{F}_2^2\Xi\left({}^G_B\mathbf{q}\right)\mathbf{b}_g \\ \mathbf{e}_1^{\mathrm{T}}\mathbf{F}_3^2\Xi\left({}^G_B\mathbf{q}\right)\mathbf{b}_g \end{bmatrix}$$

$$\begin{aligned} \nabla L^3_{\mathbf{f}_1\mathbf{f}_0\mathbf{f}_0}\mathbf{h}_d &= \begin{bmatrix} \nabla L^3_{\mathbf{f}_1\mathbf{f}_0\mathbf{f}_0}\mathbf{h}_{d1}(\mathbf{x}) \\ \nabla L^3_{\mathbf{f}_1\mathbf{f}_0\mathbf{f}_0}\mathbf{h}_{d2}(\mathbf{x}) \\ \nabla L^3_{\mathbf{f}_1\mathbf{f}_0\mathbf{f}_0}\mathbf{h}_{d3}(\mathbf{x}) \end{bmatrix} \\ &= \begin{bmatrix} \mathbf{e}_1^{\mathrm{T}}\mathbf{F}^4 & -2\mathbf{e}_1^{\mathrm{T}}\mathbf{F}_1^5 & \mathbf{e}_1^{\mathrm{T}}\mathbf{F}_1^6 \\ \mathbf{e}_1^{\mathrm{T}}\mathbf{F}^4 & -2\mathbf{e}_1^{\mathrm{T}}\mathbf{F}_2^5 & \mathbf{e}_1^{\mathrm{T}}\mathbf{F}_2^6 \\ \mathbf{e}_1^{\mathrm{T}}\mathbf{F}^4 & -2\mathbf{e}_1^{\mathrm{T}}\mathbf{F}_3^5 & \mathbf{e}_1^{\mathrm{T}}\mathbf{F}_3^6 \end{bmatrix} \end{aligned} \tag{21}$$

where

$$\begin{aligned} &\mathbf{F}^4 \triangleq \lfloor\mathbf{b}_g\rfloor_\times^2 {}^G_B\mathbf{R}^{\mathrm{T}}, \quad \mathbf{F}_i^5 \triangleq \lfloor\mathbf{b}_g\rfloor_\times^2\left(\left[\mathbf{q}_{p_i}\right]_l\Xi\left({}^G_B\mathbf{q}\right)\right)^{\mathrm{T}} \\ &\mathbf{F}_i^6 \triangleq -\left\lfloor{}^G_B\mathbf{R}^{\mathrm{T}}\Delta\mathbf{p}_i\right\rfloor_\times\lfloor\mathbf{b}_g\rfloor_\times + 2\left\lfloor\left\lfloor{}^G_B\mathbf{R}^{\mathrm{T}}\Delta\mathbf{p}_i\right\rfloor_\times\mathbf{b}_g\right\rfloor_\times. \end{aligned} \tag{22}$$

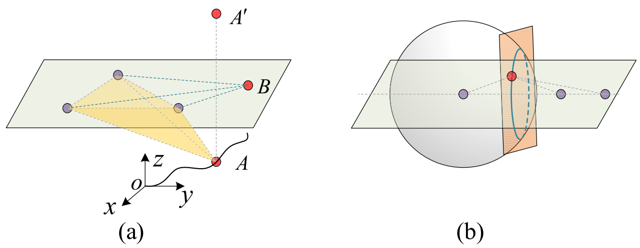

Fig. 1. Geometrical interpretation of the observability for positions. (a) Case of three noncollinear LRs. (b) Case of three collinear LRs.

The gradients of other third-order and higher order Lie derivatives are linearly dependent on the gradients of low-order Lie derivatives. Hence, by stacking nonzero and linear independent gradient matrices by row, the observability matrix $\mathbf{M}$ can be constructed, and we obtain

$$\mathbf{M}=\begin{bmatrix}\nabla L^0\mathbf{h}_d\\ \nabla L^1_{\mathbf{f}_1}\mathbf{h}_d\\ \nabla L^2_{\mathbf{f}_1\mathbf{f}_0}\mathbf{h}_d\\ \nabla L^2_{\mathbf{f}_1\mathbf{f}_2}\mathbf{h}_d\\ \nabla L^3_{\mathbf{f}_1\mathbf{f}_0\mathbf{f}_0}\mathbf{h}_d\end{bmatrix},\quad \mathbf{M}'=\begin{bmatrix}\Delta\mathbf{p}^{\mathrm{T}} & \mathbf{0}_{3\times4} & \mathbf{0}_{3\times3}\\ {}^G_B\mathbf{R}^{\mathrm{T}} & -2\mathbf{F}^0_1 & \mathbf{0}_{3\times3}\\ {}^G_B\mathbf{R}^{\mathrm{T}} & -2\mathbf{F}^0_2 & \mathbf{0}_{3\times3}\\ {}^G_B\mathbf{R}^{\mathrm{T}} & -2\mathbf{F}^0_3 & \mathbf{0}_{3\times3}\\ \mathbf{e}_1^{\mathrm{T}}\mathbf{F}^1 & -2\mathbf{e}_1^{\mathrm{T}}\mathbf{F}^2_1 & \mathbf{e}_1^{\mathrm{T}}\mathbf{F}^3_1\\ \mathbf{e}_1^{\mathrm{T}}\mathbf{F}^1 & -2\mathbf{e}_1^{\mathrm{T}}\mathbf{F}^2_2 & \mathbf{e}_1^{\mathrm{T}}\mathbf{F}^3_2\\ \mathbf{e}_1^{\mathrm{T}}\mathbf{F}^1 & -2\mathbf{e}_1^{\mathrm{T}}\mathbf{F}^2_3 & \mathbf{e}_1^{\mathrm{T}}\mathbf{F}^3_3\\ \mathbf{e}_1^{\mathrm{T}}\mathbf{F}^4 & -2\mathbf{e}_1^{\mathrm{T}}\mathbf{F}^5_1 & \mathbf{e}_1^{\mathrm{T}}\mathbf{F}^6_1\\ \mathbf{e}_1^{\mathrm{T}}\mathbf{F}^4 & -2\mathbf{e}_1^{\mathrm{T}}\mathbf{F}^5_2 & \mathbf{e}_1^{\mathrm{T}}\mathbf{F}^6_2\\ \mathbf{e}_1^{\mathrm{T}}\mathbf{F}^4 & -2\mathbf{e}_1^{\mathrm{T}}\mathbf{F}^5_3 & \mathbf{e}_1^{\mathrm{T}}\mathbf{F}^6_3\end{bmatrix}\tag{23}$$

where $\mathrm{rank}(\mathbf{M})=\mathrm{rank}(\mathbf{M}')$ and $\mathbf{M}'$ is obtained via elementary transformations on $\mathbf{M}$ (rearranging $\nabla L^1_{\mathbf{f}_1}\mathbf{h}_d$ and $\nabla L^2_{\mathbf{f}_1\mathbf{f}_2}\mathbf{h}_d$).

In the presence of three LRs, the observability conditions for systems (9) and (10) are summarized in Theorem 1.

Theorem 1: The sufficient conditions for the observability matrix $\mathbf{M}$ [i.e., (23)] to be full column rank are: 1) at least three noncollinear LRs are available; 2) FR is noncoplanar with the three noncollinear LRs; 3) the linear velocity v_x and angular velocities ω_z along the body are excited; and 4) the angular velocity bias $b_{gx}\neq 0$, and $b_{gy}\neq 0$ or $b_{gz}\neq 0$.

Proof: A detailed mathematical proof of conditions can be found in Appendix A.

The observability of the system is also interpreted from a geometric point of view. When there exists one LR and the distance between the LR and the FR is measured, it is possible for the FR to be located anywhere on a sphere; when two LRs exist, it is possible for the FR to be located anywhere on a circle; when there are three noncollinear LRs, the FR is located at one of the two discontinuous points (e.g., point A or A') or one point (e.g., point B that is coplanar with the LRs), as shown in Fig. 1(a). Hence, in the case of one or two LRs, the system is neither globally observable nor locally weakly observable for the robot's position because a point on a sphere or circle is indistinguishable from other points in the global manifold [19]. For the case of three noncollinear LRs, the system is only locally weakly observable for positions because only distinguishability in its neighbors is considered [12]. When three LRs are collinear, similar to the case with two LRs, the FR is still located on a circle [Fig. 1(b)] such that the positions of the system are unobservable.

In addition, when $v_x\neq 0$ and $\omega_z\neq 0$, significant motions can be produced and render the 3-D orientation observable. This is confirmed by detailed simulations and experiments. In addition, if conditions 1)–4) are all satisfied, the full rank of the observation matrix has shown that the angular velocity bias $\mathbf{b}_g$ is observable as shown in [13].

In particular, for the case that the FR is coplanar with the three noncollinear LRs, the FR locates at the only point (e.g., point B), as shown in Fig. 1(a), suggesting that the system is observable for positions according to the locally weakly observable definition [19]. In addition, mobile strategies of LRs are worthy of future study for condition 1).

B. State Estimator Based on ESKF

Based on the above observability analysis, the spatial configuration of the anchors and the excitations for the robot are determined, making the states able to be estimated with bounded errors. Although the traditional trilateration method can determine the position of the robot using only UWB, the sensors fusion strategy is still adopted because UWB measurements are prone to interference from the external environment, such as multipath effects [23], which may lead to positioning failures. Fusing odometry data from IMUs or wheel odometers can greatly reduce positioning errors [8], [20]. In addition, traditional trilateration methods rely on fixed anchors, while our approach can be independent of them.

To this end, an ESKF framework is employed to fuse the measurements from the reduced inertial-odometer system and the UWB for state estimation of the nonlinear system. Specifically, the true states $\mathbf{x}_t$ include the estimated states $\hat{\boldsymbol{x}}$ and error states $\tilde{\boldsymbol{x}}$. The dynamics of the estimated states are

$$\begin{aligned}{}^G_B\dot{\hat{\mathbf{p}}} &= {}^G_B\hat{\mathbf{R}}\mathbf{v}_m\\ {}^G_B\dot{\hat{\mathbf{q}}} &= \frac{1}{2}\boldsymbol{\Omega}\left(\mathbf{w}_m-\mathbf{b}_g\right){}^G_B\hat{\mathbf{q}}\\ \dot{\hat{\mathbf{b}}}_g &= \mathbf{0}.\end{aligned}\tag{24}$$

The attitude error ${}^G\tilde{\boldsymbol{\theta}}$ follows the definition of global angular error [18]:

$${}^G_B\mathbf{R}_t\approx\left(\mathbf{I}+\left\lfloor{}^G\tilde{\boldsymbol{\theta}}\right\rfloor_\times\right){}^G_B\hat{\mathbf{R}}.\tag{25}$$

Hence, the dynamics of error states can be derived as

$$\begin{aligned}{}^G_B\dot{\tilde{\mathbf{p}}} &= -\left\lfloor{}^G_B\hat{\mathbf{R}}\mathbf{v}_m\right\rfloor_\times{}^G\tilde{\boldsymbol{\theta}}-{}^G_B\hat{\mathbf{R}}\mathbf{n}_v\\ {}^G\dot{\tilde{\boldsymbol{\theta}}} &= -{}^G_B\hat{\mathbf{R}}\tilde{\mathbf{b}}_g-{}^G_B\hat{\mathbf{R}}\mathbf{n}_g\\ \dot{\tilde{\mathbf{b}}}_g &= \mathbf{n}_{wg}.\end{aligned}\tag{26}$$

The measurement Jacobian matrix corresponding to (7) is

$$\mathbf{H}_{di}=\left[\frac{\left({}^G_B\hat{\mathbf{p}}-{}^G_{Li}\mathbf{p}\right)^{\mathrm{T}}}{\left\|\left({}^G_B\hat{\mathbf{p}}-{}^G_{Li}\mathbf{p}\right)^{\mathrm{T}}\right\|_2},\quad\mathbf{0}_{1\times6}\right].\tag{27}$$

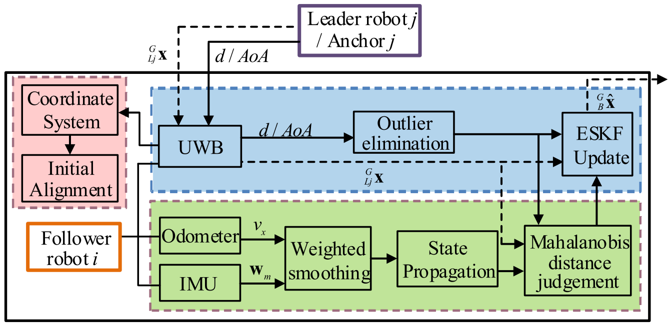

Fig. 2. System architecture from the FR$_i$'s perspective.

The discrete-time error-state transition matrix of (26) is obtained by the Euler numerical integration [18]. The remaining standard steps are omitted for brevity [18].

The architecture of the proposed UIO system is shown from the FR$_i$'s perspective in Fig. 2. The odometer and gyroscope readings from the previous and the current moments are weighted and smoothed. UWB outliers are removed twice: first by preset thresholds and, then, Mahalanobis distance [24] is calculated and compared with the threshold of Mahalanobis distance to choose whether to carry out the filter update steps. In addition, the global frame $\{\mathcal{G}\}$ is established and coupled to the initial body frame $\{\mathcal{B}\}$ of FR at first and the UWB frame is calibrated artificially to ensure precise initial alignments.

V. System With Both ToA and AoA Model

A. Observability Analysis

The observability of the proposed UIO system with both ToA and AoA measurements is also studied further. We consider one LR, and the corresponding measurement model is rewritten as

$$\mathbf{h}_a(\mathbf{x}) = {}^L_G\mathbf{R}\left({}^G_B\mathbf{p} - {}^G_L\mathbf{p}\right). \tag{28}$$

The detailed process of the observability analysis is similar to that in Section IV-A and is omitted here. By deriving the Lie derivatives and their gradients, we obtain

$$\mathbf{M} = \begin{bmatrix} \nabla L^0\mathbf{h}_a \\ \nabla L^1_{\mathbf{f}_1}\mathbf{h}_a \\ \nabla L^2_{\mathbf{f}_1\mathbf{f}_0}\mathbf{h}_a \\ \nabla L^2_{\mathbf{f}_1\mathbf{f}_1}\mathbf{h}_a \\ \nabla L^2_{\mathbf{f}_1\mathbf{f}_2}\mathbf{h}_a \\ \nabla L^3_{\mathbf{f}_1\mathbf{f}_0\mathbf{f}_0}\mathbf{h}_a \end{bmatrix}, \quad \mathbf{M}' = \begin{bmatrix} {}^G_L\mathbf{R}^{\mathrm{T}} & \mathbf{0}_{3\times 4} & \mathbf{0}_{3\times 3} \\ \mathbf{0}_{9\times 3} & -2\mathbf{F}^7 & \mathbf{0}_{9\times 3} \\ \mathbf{0}_{3\times 3} & -2\mathbf{F}^8 & \mathbf{F}^9 \\ \mathbf{0}_{3\times 3} & -2\mathbf{F}^{10} & \mathbf{F}^{11} \end{bmatrix} \tag{29}$$

where $\mathrm{rank}(\mathbf{M}) = \mathrm{rank}(\mathbf{M}')$ and $\mathbf{M}'$ is obtained via elementary transformations on the observation matrix $\mathbf{M}$. In (29),

$$\mathbf{F}^7 = \begin{bmatrix} \mathbf{F}^7_1 \\ \mathbf{F}^7_2 \\ \mathbf{F}^7_3 \end{bmatrix}, \ \mathbf{F}^8 = \begin{bmatrix} \mathbf{F}^8_1 \\ \mathbf{F}^8_2 \\ \mathbf{F}^8_3 \end{bmatrix}, \ \mathbf{F}^9 = \begin{bmatrix} \mathbf{F}^9_1 \\ \mathbf{F}^9_2 \\ \mathbf{F}^9_3 \end{bmatrix}, \ \mathbf{F}^{10} = \begin{bmatrix} \mathbf{F}^{10}_1 \\ \mathbf{F}^{10}_2 \\ \mathbf{F}^{10}_3 \end{bmatrix}$$

$$\mathbf{F}^{11} = \begin{bmatrix} \mathbf{F}^{11}_1 \\ \mathbf{F}^{11}_2 \\ \mathbf{F}^{11}_3 \end{bmatrix}. \tag{30}$$

Defining $\mathbf{r}_i = \mathbf{e}_i^{\mathrm{T}}{}^G_L\mathbf{R}^{\mathrm{T}}$, $\mathbf{q}_{\mathbf{r}_i} \triangleq [0, \mathbf{r}_i]$, we have

$$\begin{aligned} \mathbf{F}^7_i &\triangleq \left(\left[\mathbf{q}_{\mathbf{r}_i}\right]_l \Xi\left({}^G_B\mathbf{q}\right)\right)^{\mathrm{T}} \\ \mathbf{F}^8_i &\triangleq \mathbf{e}_1^{\mathrm{T}}\left(\lfloor\mathbf{b}_g\rfloor_\times\left(\left[\mathbf{q}_{\mathbf{r}_i}\right]_l \Xi\left({}^G_B\mathbf{q}\right)\right)^{\mathrm{T}}\right) \\ \mathbf{F}^9_i &\triangleq -\mathbf{e}_1^{\mathrm{T}}\left\lfloor {}^G_B\mathbf{R}^{\mathrm{T}}\mathbf{r}_i\right\rfloor_\times \\ \mathbf{F}^{10}_i &\triangleq \mathbf{e}_1^{\mathrm{T}}\left(\lfloor\mathbf{b}_g\rfloor^2_\times\left(\left[\mathbf{q}_{\mathbf{r}_i}\right]_l \Xi\left({}^G_B\mathbf{q}\right)\right)^{\mathrm{T}}\right) \\ \mathbf{F}^{11}_i &\triangleq \mathbf{e}_1^{\mathrm{T}}\left(-\left\lfloor {}^G_B\mathbf{R}^{\mathrm{T}}\mathbf{r}_i\right\rfloor_\times \lfloor\mathbf{b}_g\rfloor_\times + 2\left\lfloor \left\lfloor {}^G_B\mathbf{R}^{\mathrm{T}}\mathbf{r}_i\right\rfloor_\times \mathbf{b}_g\right\rfloor_\times\right). \end{aligned} \tag{31}$$

In the presence of one LR, the observability conditions for systems (9) and (28) are summarized in Theorem 2.

Theorem 2: The sufficient conditions for the observability matrix $\mathbf{M}$ [i.e., (29)] to be full column rank are: 1) at least one LR is available; 2) the linear velocity v_x and angular velocities ω_z along the body are excited; and 3) the angular velocity bias $b_{gx} \neq 0$, and $b_{gy} \neq 0$ or $b_{gz} \neq 0$.

Proof: A detailed mathematical proof can be found in Appendix B.

Furthermore, we analyze the observability of the system from a geometric point of view. When both ToA and AoA measurements (i.e., distance, elevation, and azimuth) from one LR are obtained, the FR's position can be uniquely determined from the output (distinguished from points in the neighborhood), suggesting that the position is observable. Similarly, v_x and ω_z need to be excited to render the 3-D orientation observable. In the same way, if conditions 1)–3) are all satisfied, the full rank of the observation matrix has shown that the angular velocity bias $\mathbf{b}_g$ is observable.

B. State Estimator Based on ESKF

Although both ToA and AoA measurements can obtain the position of FR in the body frame of LR and then directly obtain the position of FR in the global frame according to the pose of LR, the UWB measurements may not be completely reliable and may be influenced by multipath effects [23]. Fusing the odometry supplied by IMUs and wheel odometers will reduce positioning errors caused by interfered UWB measurements.

The dynamics of the estimated and error states are the same as (24)–(26). The measurement Jacobian matrix corresponding to (8) is

$$\mathbf{H}_a = \begin{bmatrix} {}^L_G\mathbf{R} & \mathbf{0}_{3\times 6} \end{bmatrix}. \tag{32}$$

In practice, the UWB modules with antenna arrays are installed on an LR, and an FR can get the AoA measurement from the neighbor LR. The orientation of the LR, i.e., ${}^L_G\mathbf{R}$, is known and transmitted to the FR. In addition, the measurement is first obtained in the UWB-AoA local frame, rather

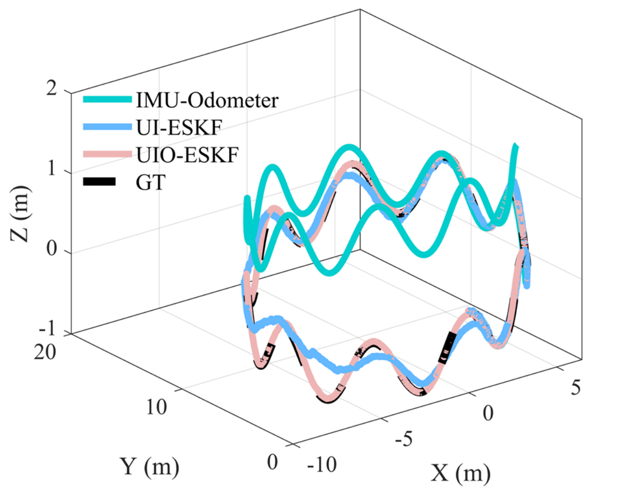

Fig. 3. Estimated trajectories of FR_1 based on different fusion approaches when UWB-distances between three LRs and FR_1 are measured. For reference, the GT is also provided.

than the LR body frame. Hence, the transformation between the body frame of the LR and the UWB-AoA local frame is calibrated manually in advance.

VI. Simulations

The proposed UIO fusion approach is evaluated in this section via MATLAB simulations. Specifically, two scenarios, i.e., UWB-distance measurements and both UWB-distance and AoA measurements, are considered. In addition, the derived local weak observability conditions are verified. The parameters used for simulations are based on the actual parameters of a low-cost IMU [28], a UWB module [29], and a wheel encoder.

A. UIO Fusion Algorithm

1) Distance Observations: Four robots, i.e., LR_1, LR_2, LR_3, and FR_1, are set up and can measure and communicate with each other. The ground truth (GT) and estimated trajectories of FR_1 are shown in Fig. 3. It reveals that the proposed UIO-ESKF approach can obtain more accurate position estimations compared to the traditional UWB-IMU fusion (UI-ESKF) approach and the dead reckoning based on the IMU-odometer method. In particular, due to the large noises of the low-cost accelerometer, the conventional UI-ESKF approach is hard to track the true trajectory accurately, while our proposed UIO-ESKF approach succeeds, which shows the advantage of replacing the low-grade accelerometer with a wheel odometer. Table I shows the mean root-mean-square error (RMSE) of pose estimations based on the three methods through 50 Monte Carlo simulations.

2) Distance and AoA Observations: In this scenario, only one LR and FR_1 are set. FR's position and attitude are observable when distance and AoA measurements are used, and v_x and ω_z are excited according to the theoretical analysis in Section V-A. The trajectory of FR_1 is estimated based on different approaches (i.e., UIO-ESKF with both distance and AoA measurements, UIO-ESKF with the distance measurement, and the IMU-odometer method). The simulation results are shown in Fig. 4, which suggests that by using both distance and AoA measurements, the proposed UIO-ESKF approach can acquire the most accurate position estimation with bounded drift errors. On the contrary, with only one LR and the corresponding distance measurement, the performance of the UIO-ESKF approach is unsatisfactory; and the error based on the IMU-odometer method inevitably diverges. The mean RMSE of pose estimations based on the three methods is also listed in Table I.

TABLE I

Position and Orientation RMSE Between Estimated States and True States Based on the IMU-Odometer Method, the UI-ESKF Method, and the UIO-ESKF Method

Type	Methods	Pos. RMSE (m)	Rot. RMSE (rad)
D	IMU-Odometer	1.265	0.151
	UI-ESKF	0.180	0.228
	UIO-ESKF	0.036	0.031
D&A	IMU-Odometer	0.914	0.125
	UIO-ESKF w/o AoA	0.308	0.057
	UIO-ESKF w/ AoA	0.148	0.050

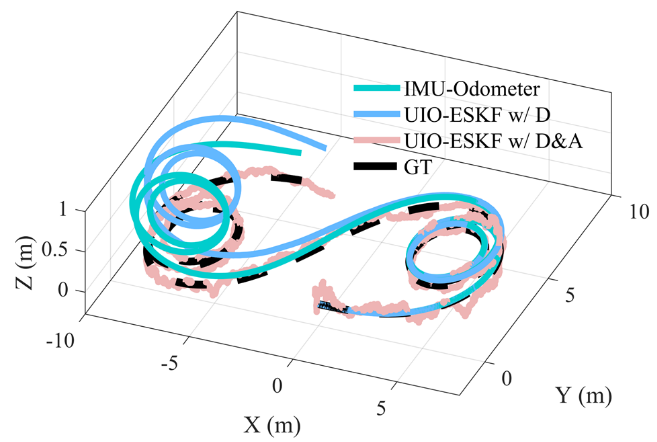

Fig. 4. Estimated trajectories of FR1 based on different fusion approaches when the distance and AoA between one LR and FR1 are measured. For reference, the GT is also provided.

TABLE II

Position and Orientation RMSE Between Estimated States and True States Based on the UIO-ESKF Method Under Different Experimental Conditions When Distance Measurements Are Used

Cases	Pos. RMSE (m)	Rot. RMSE (rad)
Collinear	0.274	0.059
Coplanar	0.145	0.038
Two anchors	0.272	0.047
Unexcitation-Static	0.010	0.269
Unexcitation-Linear	0.019	0.227
None-plane	0.035	0.046
None-uneven	0.036	0.031

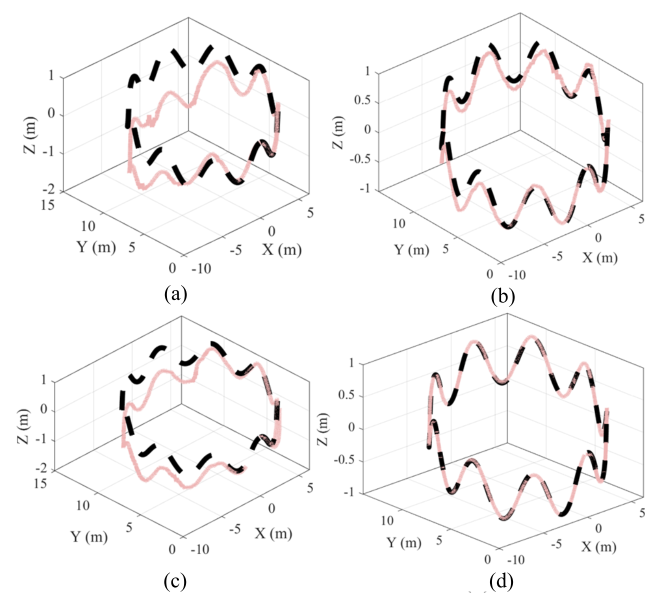

Fig. 5. Simulated and estimated trajectories based on the UIO-ESKF approach under different cases with UWB-distance measurements for verifying the position observability. (a) Three collinear anchors. (b) Three noncollinear anchors are coplanar with the robot. (c) Only two anchors. (d) All observability conditions are all satisfied.

B. Verification of Observability Conditions

To verify the position observability, estimated trajectories under different cases are shown in Fig. 5. Each case in Fig. 5(a)–(c) only violates one observability condition in Theorem 1. Whether there are two anchors or three collinear anchors, the position estimations are both unobservable and drifting errors exist. In particular, when the anchors are coplanar with the robot, the errors are mainly generated in the z-axis [seen in Figs. 5(b) and 6(f)]. However, when all observability conditions are satisfied, the position estimation can converge to the true one, which effectively demonstrates the position observability (see Table II). As for the position observability under both distance and AoA measurements, it is obvious since the measurements (i.e., distance, elevation, and azimuth angle) can uniquely determine the spatial position, which has been verified in Fig. 4.

Furthermore, we focus on the observability of the 3-D orientation of the proposed UIO system and verify it by simulating various degradation cases that fail to satisfy the observability conditions. The attitude errors along with 3σ (σ is the standard deviation) bounds are plotted in Fig. 6(a)–(e) under different cases through 50 Monte Carlo simulations. Although the error of each Monte Carlo simulation may diverge with time, the error may be positive or negative, and the mean error is generally around zero, which has little value for observability judgment. However, the standard deviation σ calculates the square root of the error, so it can be seen whether the error converges with time and then judge whether the state is observable. As shown in Fig. 6(a) and (b), when all conditions in theorem 1 are satisfied, especially $\upsilon_x \neq 0, \omega_z \neq 0$, the 3-D orientation is observable whether the robot moves on a flat surface or an uneven surface, i.e., whether ω_x and ω_y are zero. It is noted that the observability of roll angle is slightly weaker than that of pitch and yaw angle. This may be due to the fact that the axis vector corresponding to the roll angle coincides with the forward direction, that is, the direction of the linear velocity υ_x, which means that only the change of the roll angle has less influence on the change of the robot's position compared with the change of pitch and yaw angles. Fig. 6(c) shows that the roll, pitch, and yaw angles are all unobservable when the robot is static. This makes sense, because when the robot is at rest, the attitude is obtained by integrating the angular velocity and cannot be corrected indirectly by UWB measurements. Fig. 6(d) shows that the roll angle is unobservable when the robot moves in linear motion, which is intuitive because the change of roll angle under linear motion will not be reflected by UWB-distance measurements. Similarly, UWB-distance measurements also cannot reflect the yaw angle of the robot when it pirouettes, as shown in Fig. 6(e). In summary, the attitude observability is verified by the variations of the standard deviation trend in the above cases, which indicates that the linear velocity υ_x and angular velocity ω_z need to be excited simultaneously to make the 3-D orientation observable (see Table II).

As for the attitude observability under both distance and AoA measurements, through simulation, we find that the tendency of the standard deviation is consistent with those under distance measurements, which is essentially due to the same propagation model. Considering limited space, the attitude observability analysis under both distance and AoA measurements is omitted.

VII. Experiments

Real-world experiments are carried out based on commercial wheeled mobile robots, called WHEELTEC. Each robot is equipped with a Raspberry Pi, motors with encoders, a controller with an STM32F103 chip, a low-cost MPU9250-IMU [28], and a Nooploop UWB module [29]. The IMU and the encoders provide measurements at 50 Hz, and the UWB module provides distance and AoA measurements and communicates at 200 Hz. The noise density and random walk biases of the IMU are initialized according to the practical product manual. The UWB module claims a precision of ± 5 cm and $\pm 5°$. In the experiment, each robot is remotely controlled by a handle. A differential-drive model is set in the control algorithm so that the robot loses its purely lateral motion capability, thus satisfying the nonholonomic constraints. The experiments are conducted in a room, equipped with a motion capture system called Vicon that provides the GT. Fig. 7 shows the photographs of the robot platform, the uneven ground on which the robot moves, and the experiment site. The influence of sensors' extrinsic parameters on the positioning error is small and therefore ignored [8], [16]. The experiments are carried out from two aspects: one is to verify the superiority of the proposed UIO-ESKF method compared with the traditional UI-ESKF method and the other is to verify the observability conditions of the proposed UIO system.

A. UIO Fusion Algorithm

1) Distance Observations: Three noncollinear anchors were fixed in the indoor environment, and their positions were

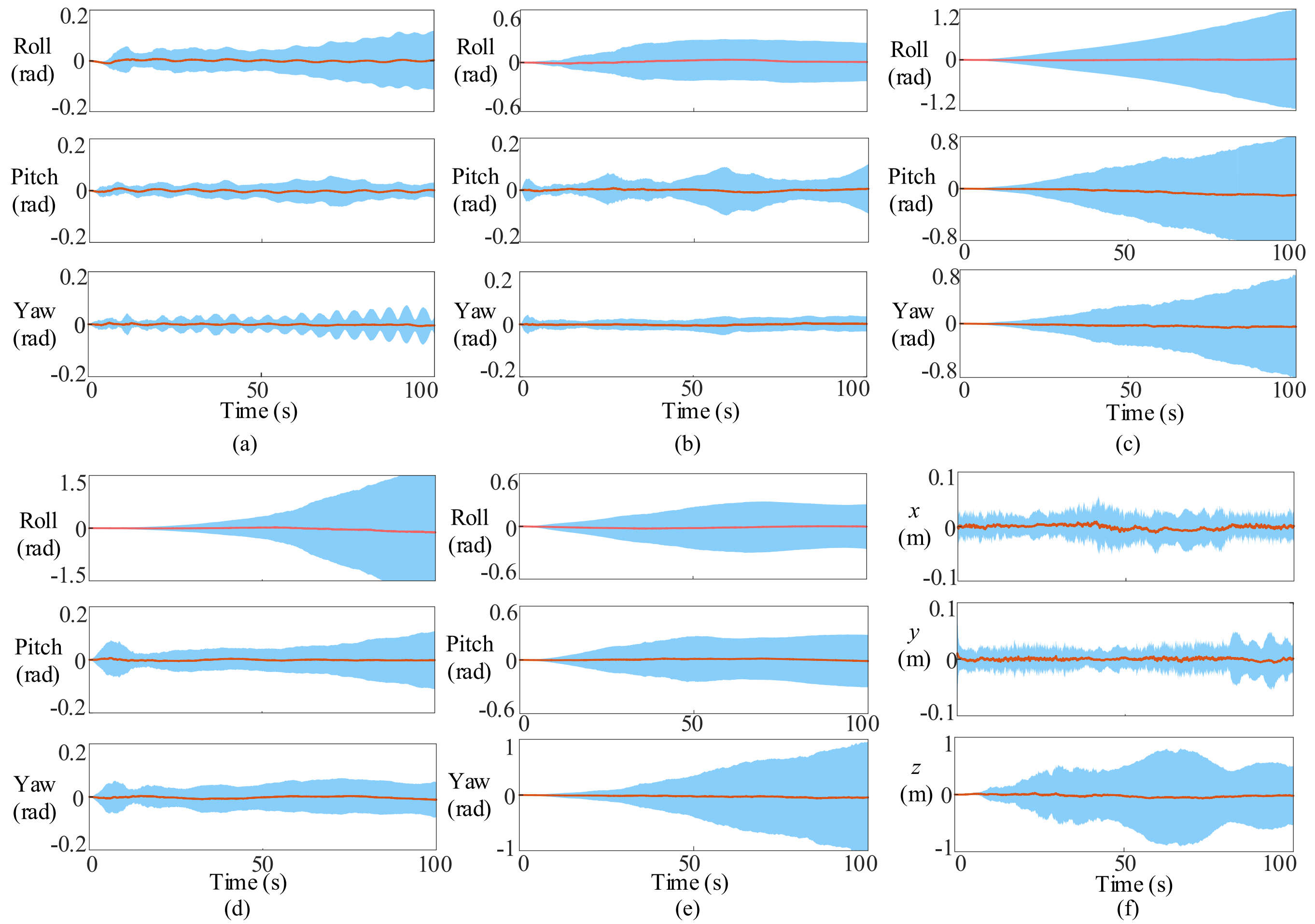

Fig. 6. Attitude or position errors along with 3σ bounds when three anchors are present and UWB-distance measurements are used. (a) Robot moves on the uneven surface, and $v_x \neq 0$ and $\omega_z \neq 0$. (b) Robot moves in a planar circular motion, and $v_x \neq 0$ and $\omega_z \neq 0$. (c) Robot is static, i.e., $v_x = 0$ and $\omega_z = 0$. (d) Robot moves in the linear motion, i.e., $v_x \neq 0$ and $\omega_z = 0$. (e) Robot rotates in place, i.e., $v_x = 0$ and $\omega_z \neq 0$. (f) Robot moves on the uneven surface, and $v_x \neq 0$ and $\omega_z \neq 0$, but it is coplanar with three LRs.

precisely calibrated to be (−1.94, 0.42, 1.26) m, (1.69, 2.03, 1.26) m, and (1.81, −1.22, 1.26) m. Fig. 8 shows the overview of the six tests, three of which were performed on smooth ground [Fig. 8(a)–(c)] and the other three were performed on the uneven ground full of stones [Fig. 8(d) and (e)], as shown in Fig. 7(b). Specifically, the true trajectory from Vicon and the estimated trajectories based on both the proposed UIO-ESKF approach and the conventional UI-ESKF approach are displayed and compared. In terms of the UI-ESKF approach, the IMU-only propagation model [5], [18], [25] is used, that is, both acceleration and angular velocity information are adopted, and UWB measurements are tightly coupled with IMU measurements. Obviously, due to the large noises of the low-cost accelerometer, the estimated trajectory based on the conventional UI-ESKF approach fluctuates significantly, which is more terrible on the bumpy ground, while the estimated trajectory based on our proposed method is smoother and agrees better with the GT provided. Essentially, the reason for the great jitter of the trajectory based on the UI-ESKF method is that there is no observation of the velocity although the robot's position was constrained by the UWB measurements. In this way, direct integration of noisy acceleration data will produce unstable position jitter, especially during sharp motion. In addition, it was found in the experiment that the fluctuation was particularly prominent when the velocity changed greatly. The absolute trajectory error (ATE) [26] is used to calculate and evaluate the accuracy of the positioning methods. The ATE for two approaches under different trajectories in 3-D space is shown in Table III. The results reveal that the average ATE of six field tests, i.e., trajectories (a)–(f), based on the proposed UIO-ESKF approach is 0.09 m, while the average ATE based on the UI-ESKF approach is 0.92 m, which indicates the outstanding performance of the UIO fusion approach compared with the UWB-IMU fusion.

2) Distance and AoA Observations: By incorporating the AoA measurement, only one anchor is required to assist the FR. In this experiment, due to the limitations of the commercial UWB hardware used, the AoA measurement can only contain distance and azimuth angle, so LR and FR are set to move in the same plane such that we assume that the measured elevation angle is zero. The anchor with UWB antenna arrays is located in (−2.6, 0, 0.34) m. Fig. 9(a)–(d) shows that after fusing both distance and AoA measurements, the proposed UIO-ESKF approach performed satisfactorily in terms of the drift error compared to the UIO-ESKF approach with distance measurements, validating the observability analysis results that

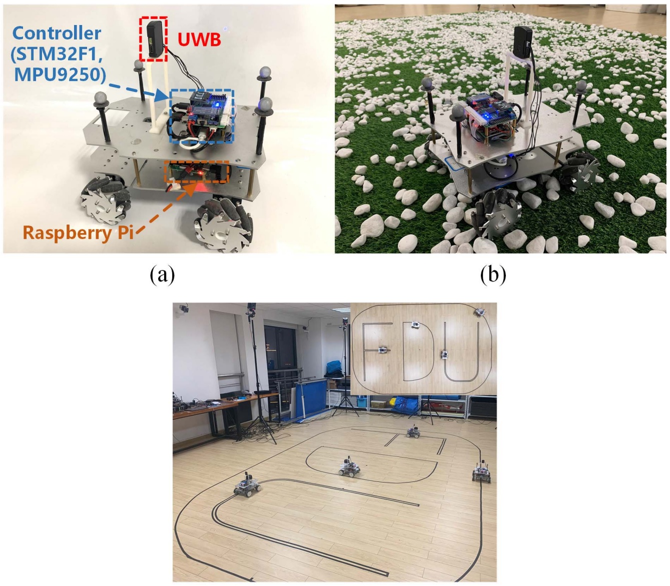

Fig. 7. (a) Wheeled robot platform used in experiments. (b) Uneven ground surface on which the robot moves. (c) Experiment site equipped with a motion capture system.

TABLE III
ATE of Various Trajectories Based on the UIO-ESKF Approach and the UI-ESKF Approach in 3-D Space When UWB-Distance Measurements Are Used in the Field Tests

ATE	UIO-ESKF	UI-ESKF
Trajectory (a)	0.104	0.740
Trajectory (b)	0.104	1.096
Trajectory (c)	0.079	1.009
Trajectory (d)	0.069	0.687
Trajectory (e)	0.086	1.077
Trajectory (f)	0.094	0.922

TABLE IV
ATE of the Various Trajectories in 3-D Space Based on the UIO-ESKF Approach With Distance and AoA Measurements and the UIO-ESKF Approach With Distance Measurements

ATE	UIO-ESKF w/ D&A (m)	UIO-ESKF w/ D (m)
Trajectory (a)	0.161	.1.060
Trajectory (b)	0.106	0.459
Trajectory (c)	0.097	0.171
Trajectory (d)	0.168	0.747

only one LR can guarantee accurate position estimation with bounded errors. The ATE based on the two approaches for the trajectories in Fig. 9 is listed in Table IV. The incorporation of AoA greatly reduced the estimation error, and the average estimation accuracy is 0.133 m. In summary, although the measurement accuracy of the AoA angle is slightly worse than that of the distances in practice, which is reflected in more noise and fluctuation in the green line in Fig. 9, the number of the

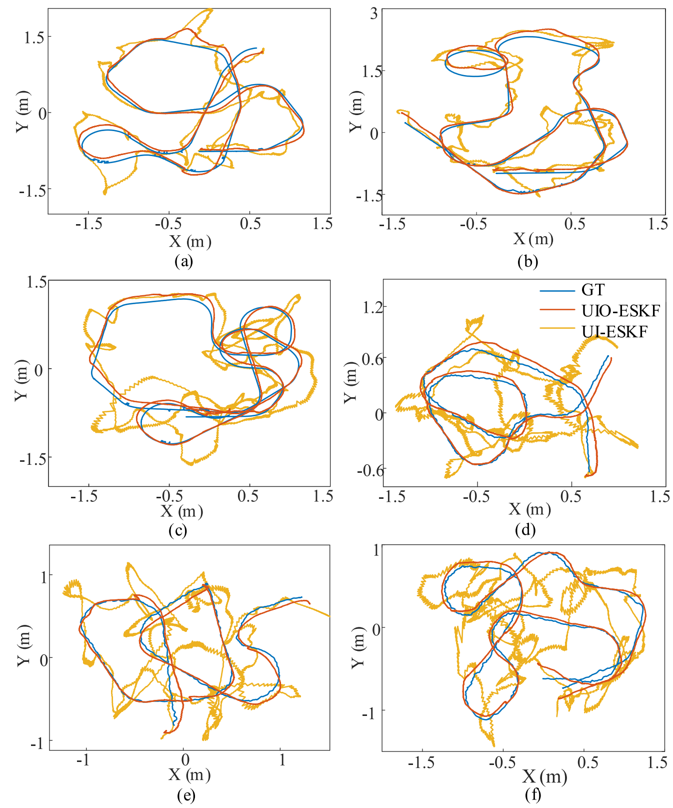

Fig. 8. Estimated trajectories based on different approaches when UWB-distance measurements were used. (a)–(c) Robot moved on the 2-D plane. (d)–(f) Robot moved on the uneven surface. For reference, the GT is also provided by Vicon.

anchors is reduced, and the positioning accuracy after fusion is close to that using three-anchor distance measurements.

B. Verification of Observability Conditions

The accurate position estimations of the robot have verified the position observability in Section VII-A. For UWB-distance observations, three noncollinear anchors make the position to be observable. For both distance and AoA observations, one anchor ensures that the position estimation converges to the true values. For degradation cases where the position is unobservable, the estimated trajectories based on the UIO fusion approach in Fig. 10(a) and (b) indicate that the robot's position cannot be determined by using three collinear anchors or only two anchors, which is consistent with the theoretical analysis and the simulation. Their corresponding ATEs are 0.353 m [Fig. 10(a)] and 0.196 m [Fig. 10(b)]. In addition, when the robot is coplanar with three noncollinear anchors, the estimated trajectory is shown in Fig. 10(c) and the position errors along the x-, y-, and z-axes are shown in Fig. 11(b). For comparisons, the position errors of the trajectory in Fig. 8(a) based on the UIO-ESKF approach are also given in Fig. 11(a). At this time, since the UWB measurements had little information about the z-position and the geometric dilution of precision (GDOP) was poor, large errors along the z-axis are generated for the coplanar case, as shown in Fig. 11(b). The corresponding ATE of trajectory in Fig. 10(c) was 0.185 m. Furthermore, the attitude observability is analyzed and verified

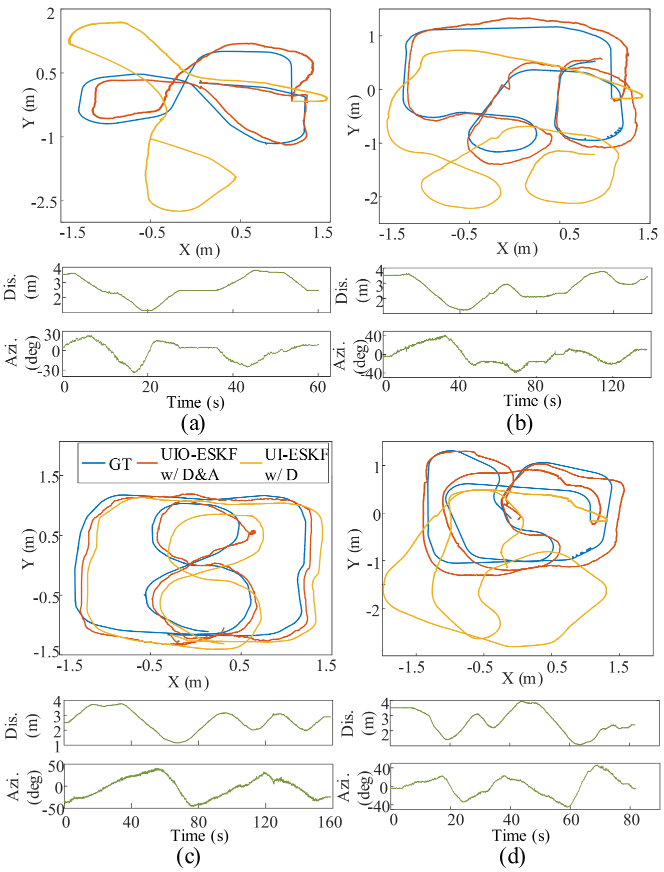

Fig. 9. Estimated trajectories based on different approaches and when both distance and AoA measurements were used during the experiments. For each subgraph, the upper graph represents the estimated trajectories, and the second and third are, respectively, the distance and AoA measurements. For reference, the GT is also provided by Vicon.

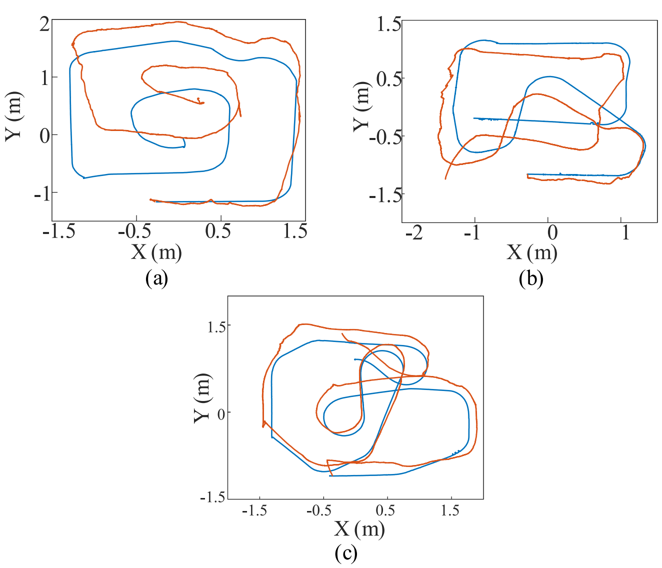

Fig. 10. Estimated trajectories based on the proposed UIO-ESKF approach when UWB-distance measurements were used. Blue lines represent the true trajectory and orange lines represent the estimated trajectory. (a) Three anchors are collinear. (b) Only two anchors are used. (c) Robot is coplanar with three noncollinear anchors.

in the following, and three degradation cases are tested. Since both the linear velocity v_x and the angular velocity ω_z need to be excited to make the 3-D attitude observable, three types of tests for the degradation scenarios are performed, i.e., static state ($v_x = 0, \omega_z = 0$), pirouette ($v_x = 0, \omega_z \neq 0$), and linear motion ($v_x \neq 0, \omega_z = 0$). At this time, three anchors are used to provide the distance measurements, which first guarantees the position observability. The 3-D attitude errors (yaw, pitch, and roll errors) between the estimated values and true values are shown in Fig. 12. When the robot is stationary, the estimated roll, pitch, and yaw angles all gradually diverge and the error accumulates over time, as shown in Fig. 12(a). When the robot spins in place, the position is still unchanged, and thus, the yaw angle obtained by integrating ω_z is unable to be observed by UWB measurements and the yaw error accumulates gradually, as shown in Fig. 12(b). When the robot moves along one line, the roll angle is hard to be observable, shown in Fig. 12(c), because the axis vector of roll angle coincides with the direction of linear motion, which means that the change in the roll angle cannot be reflected by the change in the robot's position or UWB-distance measurements.

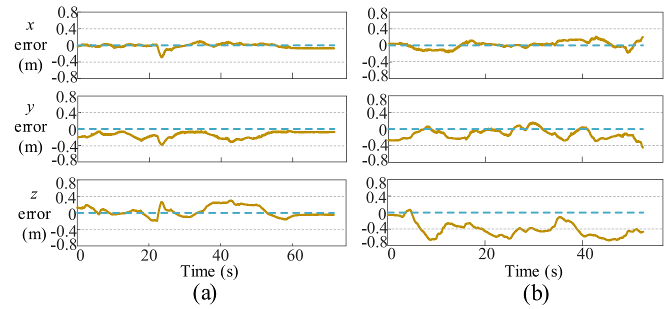

Fig. 11. Position errors (a) when the robot is not coplanar with three noncollinear anchors and (b) when the robot is coplanar with three noncollinear anchors.

Meanwhile, when both the linear velocity v_x and the angular velocity ω_z are motivated, the 3-D orientation errors based on the UIO fusion approach are shown in Fig. 13, where Fig. 13(a) shows the attitude errors of trajectory (a) in Fig. 8, i.e., motion on a plane, and Fig. 13(b) shows the attitude errors of trajectory (d) in Fig. 8, i.e., motion on an uneven surface. It can be seen that the attitude error converges to zero and does not diverge over time no matter on the plane or rugged ground. The corresponding 3-D attitude RMSE, which is the Euclidean distance between the Euler angles defined in [27], is calculated as 0.090 rad [Fig. 13(a)] and 0.150 rad [Fig. 13(b)]. If only the yaw error is considered, the corresponding errors are 0.052 and 0.059 rad. Not only that, when the initial yaw angle was set as a wrong value, the estimated yaw angle could still converge to the true value quickly, as shown in the green region in Fig. 13(b). These results effectively confirm the observability of the 3-D attitude. For both distance and AoA observations, when $v_x \neq 0$ and $\omega_z \neq 0$, the attitude errors of trajectory (c) in Fig. 9 are shown in Fig. 13(c), and the calculated 3-D attitude RMSE is 0.168 rad and the yaw error is 0.062 rad. From the trend of errors with time, we can find that the 3-D orientation is observable when the observability conditions under both distance and AoA measurements are satisfied.

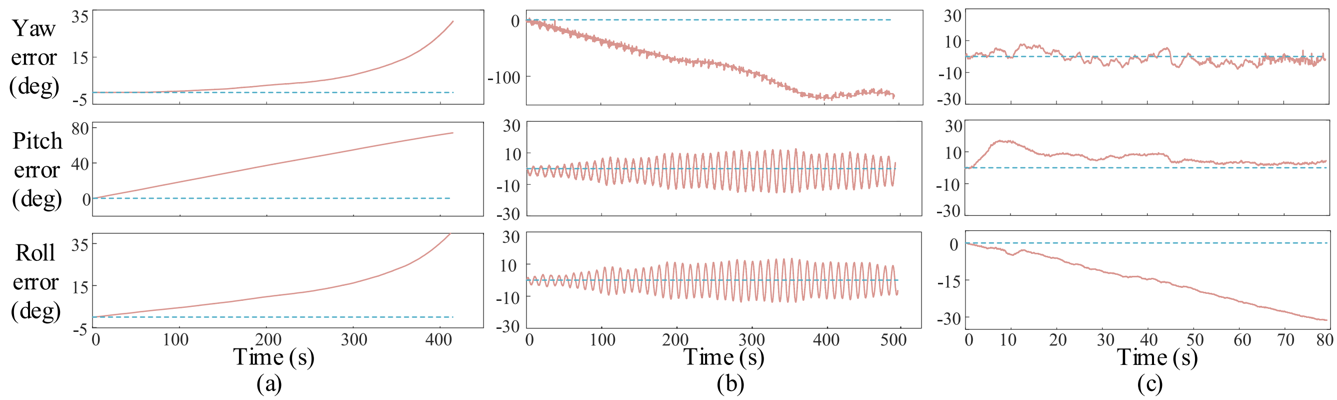

Fig. 12. Attitude errors when three anchors are present and UWB-distance measurements are used. (a) Robot is static, i.e., $v_x = 0$ and $\omega_z = 0$. (b) Robot rotates in place, i.e., $v_x = 0$ and $\omega_z \neq 0$. (c) Robot moves in the linear motion, i.e., $v_x \neq 0$ and $\omega_z = 0$.

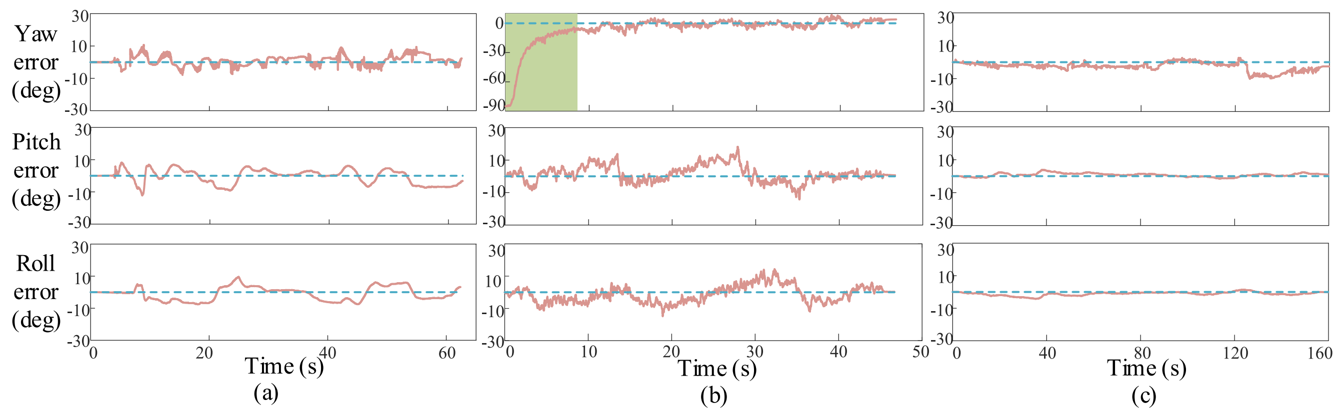

Fig. 13. Attitude errors when $v_x \neq 0$ and $\omega_z \neq 0$. (a) Attitude errors when UWB-distance measurements are used (three anchors) and the robot moves on the plane. (b) Attitude errors when UWB-distance measurements are used (three anchors) and the robot moves on the uneven surface full of stones. (c) Attitude errors when distance and AoA measurements (one anchor) are used and the robot moves on the plane.

C. Multirobot Positioning Tests

When some of the multirobots can obtain accurate global poses, they can play the role of the moving anchors to assist the rest of the robots in positioning. In the experiment, the LRs' true global poses were captured by the motion capture system as known values and subscribed by other FRs. In the actual scenes, especially in the unknown environments, the estimation values from high-precision SLAM algorithms can be used as an alternative to replacing the results of the motion capture system.

Five experiments are performed to test the effectiveness of our approach when using LRs instead of anchors. Fig. 14 shows the estimated trajectories of the FR (along the outermost shape) from one of five experiments when three LRs moved along the letters, i.e., "F," "D," and "U" and UWB-distance measurements are used, as shown in Fig. 7(c). The average ATEs of five tests based on the UIO-ESKF method and the UI-ESKF method are, respectively, calculated as 0.358 and 0.717 m. The position error is mostly along the z-axis, and the maximum error in the z-direction is 1.355 m based on the UIO-ESKF approach in Fig. 14, but no outliers are found in the UWB-distance measurements at this time, which illustrates that the errors resulted from the fact that the FR is coplanar with three LRs. Assuming that the errors in the z-axis are not considered, the average ATE of the estimated values in the

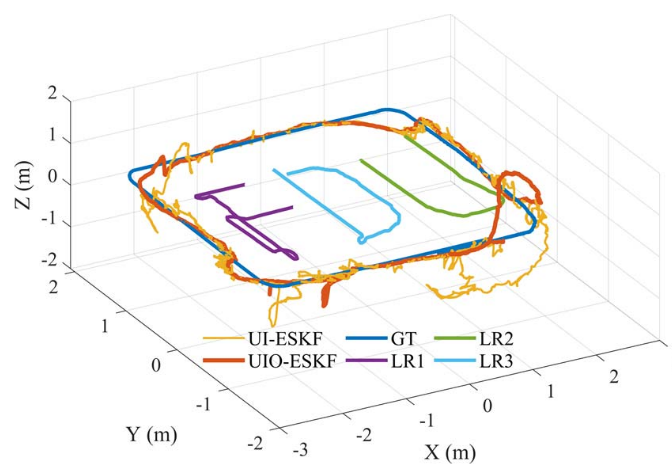

Fig. 14. Estimated trajectories based on different approaches when UWB-distance measurements are used. For reference, the GT is also provided by Vicon.

xoy plane is calculated as 0.259 m (UIO-ESKF) and 0.472 m (UI-ESKF). On the other hand, the average attitude errors of five tests based on the UIO-ESKF method and the UI-ESKF method are, respectively, 0.422 and 0.355 rad. The attitude error is mostly from the roll and pitch angle for the UIO-ESKF approach and is greater than the error in Fig. 13(a) and (b).

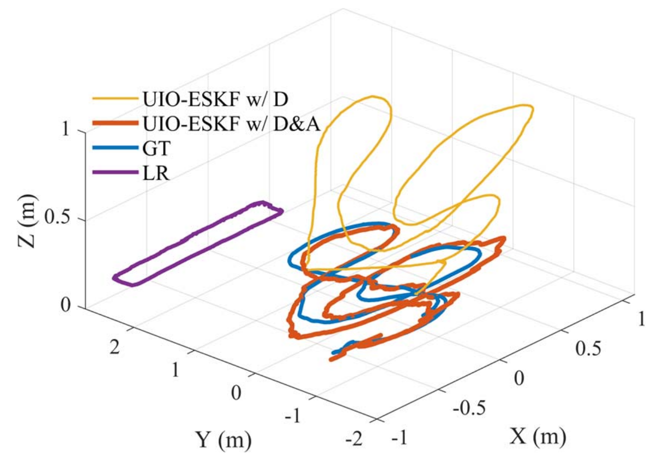

Fig. 15. Estimated trajectories based on both distance and AoA measurements and distance-only measurements during the experiments. For reference, the GT is also provided by Vicon.

The reason for the large attitude error is that the FR's trajectory is mainly linear motions, and the movement speed is slow, which makes the excitation of attitude observability insufficient. If only the yaw error is considered, the average RMSE of yaw is 0.106 and 0.353 rad. For the UI-ESKF method, the 2-D attitude error is close to the 3-D attitude error essentially because three-axis acceleration information is helpful for roll and pitch angles to be observable. In addition, we find that the estimated trajectories based on the UI-ESKF method do not fluctuate much compared with those in Fig. 8, which may be due to the slow movement and no drastic speed change in this process.

In addition, when only one LR exists and both distance and AoA measurements are used, six experiments are performed. The estimated trajectories from one of six experiments are shown in Fig. 15, in which LR follows a rectangular shape and FR follows a musical note shape. Obviously, the estimated trajectory based on the UIO-ESKF approach with both distance and AoA measurements agrees better with the true trajectory compared with that using distance measurements. The average ATEs of six experiments based on the UIO-ESKF method with both distance and AoA measurements and the UIO-ESKF method with distance measurements are 0.13 and 0.226 m, respectively, and the average attitude RMSEs of six experiments are 0.149 and 0.247 rad. These results demonstrate that only one LR and the corresponding distance and AoA measurements can guarantee the FR's position observability, while one LR and the corresponding distance measurements cannot. Furthermore, we speculate that the position observability is a prerequisite for attitude observability for this system. Since the position cannot be determined using one LR and the corresponding distance measurements, even if υ_x and ω_z are excited, the Euler angles cannot be indirectly determined by the changes of the position.

In summary, these two kinds of experiments on multirobot localization illustrate that when the true global poses of LRs are known and the observability conditions are satisfied, they can assist the other FRs in localization although the positioning accuracy is slightly inferior to using static anchors.

VIII. Conclusion

In this article, we propose a novel UIO fusion localization scheme in GPS-denied environments. Rather than the INS that calls for high-precision accelerometers, the wheel odometer is employed and integrated with the gyroscope to propagate the system state, enabling low-cost IMUs usable in this approach. We analyze the observability property of the proposed UIO system with different measurement models for nonholonomic ground robots, which reveals that to ensure locally weakly observable for positions, at least three noncollinear anchors/LRs are required to assist FRs when using the ToA measurement model and one LR is required when using the both ToA and AoA measurement model. Furthermore, the linear velocity along the body x-axis and the angular velocity along the body z-axis are excited in such a way that the 3-D orientation can be observable. In summary, the proposed scheme has a few advantages and values. First, the proposed UIO-fusion solves the problem of tightly coupled UI-fusion, i.e., large drifts caused by low-cost IMUs. The localization performance based on the UIO-ESKF approach outperforms the previous UWB-IMU fusion or IMU-odometer fusion methods, and the feasibility and effectiveness are verified through simulation and experiments. Second, the observability conditions of the 3-D position and attitude for the proposed UIO system are theoretically determined and experimentally verified, and the degenerate cases where the states cannot be observed are enumerated, making the scheme complete. Third, it has a wider application range than traditional triangulation methods because not only static anchors but also moving LRs can be used as absolute known information to assist robots in localization. However, it is worth noting that only forward velocity from the wheel odometer is utilized, and the error may drift when the wheels slip in the proposed UIO fusion scheme. Future study will focus on adding lateral and vertical velocities observations for correcting drift errors and establishing more accurate robot motion models to compensate for wheel slippage.

Appendix A

In this section, we provide a mathematical proof of Theorem 1. We consider three LRs, and their positions are denoted as ${}^G_{L_i}\mathbf{p} = [{}^G_{L_i}x, {}^G_{L_i}y, {}^G_{L_i}z]^{\mathrm{T}}, i = 1, 2, 3$. Since the global frame can be set up arbitrarily, which does not affect the observability of the system, therefore, to simplify the proof, the body center of LR_1 is chosen as the origin of the global frame (i.e., ${}^G_{L_1}x = 0, {}^G_{L_1}y = 0$ and ${}^G_{L_1}z = 0$). The x-axis is set to follow the direction from LR_1 to LR_2. As a result, ${}^G_{L_2}x \neq 0$, ${}^G_{L_2}y = 0$ and ${}^G_{L_2}z = 0$ (${}^G_{L_2}x \neq {}^G_{L_1}x$ because the overlapping of multiple LRs is regarded as one LR). Then, we determine the y-axis so that LR_3 also sits on the xoy plane, which means that ${}^G_{L3}z = 0$.

Furthermore, we use the Gaussian elimination to prove the full rank of the observation matrix (23). We separately consider the conditions for the full rank of the three columns of (23). The first column has full column rank if $\Delta\mathbf{p}^{\mathrm{T}}$ is full rank, so we first compute the determinant of $\Delta\mathbf{p}^{\mathrm{T}}$

$$\left|\Delta\mathbf{p}^{\mathrm{T}}\right| = {}^G_{L_2}x\,{}^G_{L_3}y\,{}^G_{B}z \tag{33}$$

where $|\cdot|$ represents matrix determinant. Since ${}^G_{L_2}x \neq 0$, the conditions for $\Delta\mathbf{p}^{\mathrm{T}}$ to be full rank are ${}^G_{L_3}y \neq 0$ and ${}^G_{B}z \neq 0$. Here, ${}^G_{L_3}y \neq 0$ means that LR_3 cannot be collinear with LR_2 or LR_1, which results in condition 1) in Theorem 1. ${}^G_{B}z \neq 0$ indicates that FR cannot be coplanar with the three noncollinear LRs, which gives rise to condition 2) in Theorem 1. Therefore, if conditions 1) and 2) are satisfied, the first column of $\mathbf{M}'$ has a full rank (the rank equals 3). Now, we can use the first row of (23) to eliminate the first column of the other rows of (23) through Gaussian elimination.

Second, rows 2–4 in column 2 of $\mathbf{M}'$ form a 9×4 matrix, denoted by $\mathbf{F}^0$. After taking four rows from $\mathbf{F}^0$ and calculating their determinant, we have

$$\det(1,2,4,7) = 16{}^G_{L_2}x{}^G_{L_3}y{}^G_{B}z\left(r_{13}{}^G_{B}x + r_{23}{}^G_{B}y + r_{33}{}^G_{B}z\right) \tag{34}$$

$$\det(1,4,5,7) = 16{}^G_{L_2}x{}^G_{L_3}y{}^G_{B}z\left(r_{13}\Delta x_2 + r_{23}{}^G_{B}y + r_{33}{}^G_{B}z\right) \tag{35}$$

$$\det(1,4,7,8) = 16{}^G_{L_2}x{}^G_{L_3}y{}^G_{B}z\left(r_{13}\Delta x_3 + r_{23}\Delta y_3 + r_{33}{}^G_{B}z)\right) \tag{36}$$

where

$$\Delta x_2 = {}^G_{B}x - {}^G_{L_2}x, \quad \Delta x_3 = {}^G_{B}x - {}^G_{L_3}x, \;\; \Delta y_3 = {}^G_{B}y - {}^G_{L_3}y \tag{37}$$

and r_{ij} represents the ith row and the jth column of the matrix ${}^G_{B}\mathbf{R}$. $\det(1,2,4,7)$ denotes the determinant of the matrix consisting of the first, second, fourth, and seventh rows of $\mathbf{F}^0$. Similarly, so are (35) and (36).

We prove by contradiction that the matrix of $\mathbf{F}^0$ has full column rank. First, we assume that all three determinants, i.e., (34)–(36), are equal to 0. When (34) is zero, we can obtain

$$r_{13}{}^G_{B}x + r_{23}{}^G_{B}y + r_{33}{}^G_{B}z = 0. \tag{38}$$

Substituting it into (35) and (36), we have

$$\det(1,4,5,7) = -16{}^G_{L_2}x^2{}^G_{L_3}y{}^G_{B}z r_{13} = 0 \Rightarrow r_{13} = 0. \tag{39}$$

Furthermore, substituting (38) and (39) into (36), we have

$$\det(1,4,7,8) = -16{}^G_{L_2}x{}^G_{L_3}y^2{}^G_{B}z r_{23} = 0 \Rightarrow r_{23} = 0. \tag{40}$$

Finally, substituting $r_{13} = 0$, $r_{23} = 0$, and ${}^G_{B}z \neq 0$ into (38), we find that $r_{33} = 0$, which violates the full rank of the rotation matrix ${}^G_{B}\mathbf{R}$. Therefore, the assumption does not hold, that is, the three determinants cannot be all zero. This means that $\mathbf{F}^0$ has a full column rank, i.e., the second column of $\mathbf{M}'$ has a full rank (rank is equal to 4). It is worth noting that rows 1, 4, and 7 of $\mathbf{F}^0$ correspond to the excitation of v_x, and rows 2, 5, and 8 correspond to the excitation of ω_z, which indicates that the sufficient condition for the full column rank of $\mathbf{F}^0$ is that v_x and ω_z are both excited at the same time. Now, we can eliminate the second column of the remaining rows of (23) with $\mathbf{F}^0$.

Similarly, we extract the last three rows of the last column of the matrix $\mathbf{M}'$ and construct it as a new matrix, denoted by $\mathbf{F}^6$. Its determinant yields

$$|\mathbf{F}^6| = 2{}^G_{L_2}x{}^G_{L_3}y{}^G_{B}z b_{gx}\left(b_{gy}^2 + b_{gz}^2\right). \tag{41}$$

Since ${}^G_{L_2}x{}^G_{L_3}y{}^G_{B}z \neq 0$, the conditions for $\mathbf{F}^6$ to be full rank are that the angular velocity bias $b_{gx} \neq 0$, and $b_{gy} \neq 0$ or $b_{gz} \neq 0$, which result in condition 4) in Theorem 1. Note that the angular velocity bias is one of the mechanical properties of the gyroscope, which is affected by the ambient temperature and varies each time the gyroscope is energized. Thus, in general, the bias is not 0. At this time, the third column of the remaining rows of (23) can be eliminated with $\mathbf{F}^6$ through Gaussian elimination. Finally, the observation matrix (23) can be reduced to a full rank identity matrix.

Appendix B

In this section, we provide a mathematical proof of Theorem 2. For the first column of (29), first, the rotation matrix ${}^G_{L}\mathbf{R}^{\mathrm{T}}$ is full rank, so the first column is full rank (rank is equal to 3). ${}^G_{L}\mathbf{R}^{\mathrm{T}}$ is actually derived from accurate known information. Therefore, it corresponds to condition 1) in Theorem 2. Now, we can use the first row of (29) to eliminate the first column of the other rows of (29) through Gaussian elimination.

Besides, for the second column of (29), we extract four rows from the 9×4 matrix $\mathbf{F}^7$ and calculate their determinant, i.e.,

$$\begin{aligned}
\det(1,2,4,7) &= 16\left({}^L_G\mathbf{R}{}^G_B\mathbf{R}\right)_{[1,3]} = 16\left({}^L_B\mathbf{R}\right)_{[1,3]}\\
\det(1,4,5,7) &= -16\left({}^L_G\mathbf{R}{}^G_B\mathbf{R}\right)_{[2,3]} = -16\left({}^L_B\mathbf{R}\right)_{[2,3]}\\
\det(1,4,7,8) &= 16\left({}^L_G\mathbf{R}{}^G_B\mathbf{R}\right)_{[3,3]} = 16\left({}^L_B\mathbf{R}\right)_{[3,3]}
\end{aligned} \tag{42}$$

where the subscript $[i, j]$ denotes the ith row and the jth column of the matrix. Since the third column of any rotation matrix cannot all be zero, it shows that $\mathbf{F}^7$ has a full column rank. Similarly, rows 1, 4, and 7 of $\mathbf{F}^7$ correspond to the excitation of v_x, and rows 2, 5, and 8 correspond to the excitation of ω_z, which indicates that the sufficient condition for the full column rank of $\mathbf{F}^7$ is that v_x and ω_z are both excited at the same time. At this time, we can eliminate the second column of the remaining rows of (29) with $\mathbf{F}^7$.

Furthermore, for the third column of (29), we can find that the determinant of $\mathbf{F}^{11}$ is equal to $2b_{gx}(b_{gy}^2 + b_{gz}^2)$, which indicates that when $b_{gx} \neq 0$ and $b_{gy} \neq 0$ or $b_{gz} \neq 0$, the third column is also full rank. This gives rise to condition 3) in Theorem 2. The third column of the remaining rows of (29) can be eliminated with $\mathbf{F}^{11}$ through Gaussian elimination. Finally, the observation matrix (29) can be reduced to a full rank identity matrix.

Acknowledgment

The authors would like to thank Kaiwen Yu, Bin Huang, and Hongsen Pang for their assistance in experiments.

References

[1] M. Zhong, J. Guo, and Z. Yang, "On real time performance evaluation of the inertial sensors for INS/GPS integrated systems," *IEEE Sensors J.*, vol. 16, no. 17, pp. 6652–6661, Sep. 2016, doi: 10.1109/JSEN.2016.2588140.

[2] R. Yang, X. Yang, J. Wang, M. Zhou, Z. Tian, and L. Li, "Decimeter level indoor localization using WiFi channel state information," *IEEE Sensors J.*, vol. 22, no. 6, pp. 4940–4950, Mar. 2022, doi: 10.1109/JSEN.2021.3067144.

[3] Y. Zhang, X. Tan, and C. Zhao, "UWB/INS integrated pedestrian positioning for robust indoor environments," *IEEE Sensors J.*, vol. 20, no. 23, pp. 14401–14409, Dec. 2020, doi: 10.1109/JSEN.2020.2998815.

[4] W. Shule, C. M. Almansa, J. P. Queralta, Z. Zou, and T. Westerlund, "UWB-based localization for multi-UAV systems and collaborative heterogeneous multi-robot systems," *Proc. Comput. Sci.*, vol. 175, pp. 357–364, 2020, doi: 10.1016/j.procs.2020.07.051.

[5] W. You, F. Li, L. Liao, and M. Huang, "Data fusion of UWB and IMU based on unscented Kalman filter for indoor localization of quadrotor UAV," *IEEE Access*, vol. 8, pp. 64971–64981, 2020, doi: 10.1109/ACCESS.2020.2985053.

[6] J. Li, Y. Bi, K. Li, K. Wang, F. Lin, and B. M. Chen, "Accurate 3D localization for MAV swarms by UWB and IMU fusion," in *Proc. IEEE 14th Int. Conf. Control Autom. (ICCA)*, Jun. 2018, pp. 100–105, doi: 10.1109/ICCA.2018.8444329.

[7] A. Goudar and A. P. Schoellig, "Online spatio-temporal calibration of tightly-coupled ultrawideband-aided inertial localization," in *Proc. IEEE/RSJ Int. Conf. Intell. Robots Syst. (IROS)*, Sep. 2021, pp. 1161–1168, doi: 10.1109/IROS51168.2021.9636625.

[8] M. Li, H. Zhu, S. You, and C. Tang, "UWB-based localization system aided with inertial sensor for underground coal mine applications," *IEEE Sensors J.*, vol. 20, no. 12, pp. 6652–6669, Jun. 2020, doi: 10.1109/JSEN.2020.2976097.

[9] Y. Cao, C. Yang, R. Li, A. Knoll, and G. Beltrame, "Accurate position tracking with a single UWB anchor," in *Proc. IEEE Int. Conf. Robot. Autom. (ICRA)*, May 2020, pp. 2344–2350, doi: 10.1109/ICRA40945.2020.9197345.

[10] Y. Wang and X. Li, "The IMU/UWB fusion positioning algorithm based on a particle filter," *ISPRS Int. J. Geo-Information*, vol. 6, no. 8, p. 235, Aug. 2017, doi: 10.3390/ijgi6080235.

[11] M. Brossard, A. Barrau, and S. Bonnabel, "RINS-W: Robust inertial navigation system on wheels," in *Proc. IEEE/RSJ Int. Conf. Intell. Robots Syst. (IROS)*, Nov. 2019, pp. 2068–2075, doi: 10.1109/IROS40897.2019.8968593.

[12] J. Kelly and G. S. Sukhatme, "Visual-inertial sensor fusion: Localization, mapping and sensor-to-sensor self-calibration," *Int. J. Robot. Res.*, vol. 30, no. 1, pp. 56–79, 2011, doi: 10.1177/0278364910382802.

[13] A. Goudar, K. Pereida, and A. P. Schoellig, "Ultra-wideband aided inertial navigation: Observability analysis and sensor extrinsics calibration," in *Proc. IEEE Int. Conf. Intell. Robot. Syst.*, Mar. 2020, pp. 1–7. [Online]. Available: http://www.dynsyslab.org.

[14] X. Xia, E. Hashemi, L. Xiong, A. Khajepour, and N. Xu, "Autonomous vehicles sideslip angle estimation: Single antenna GNSS/IMU fusion with observability analysis," *IEEE Internet Things J.*, vol. 8, no. 19, pp. 14845–14859, Oct. 2021, doi: 10.1109/JIOT.2021.3072354.

[15] B. Araki et al., "Range-based cooperative localization with nonlinear observability analysis," in *Proc. IEEE Intell. Transp. Syst. Conf. (ITSC)*, Oct. 2019, pp. 1864–1870, doi: 10.1109/ITSC.2019.8916915.

[16] A. Martinelli and R. Siegwart, "Observability analysis for mobile robot localization," in *Proc. IEEE/RSJ Int. Conf. Intell. Robots Syst.*, Aug. 2005, pp. 1471–1476, doi: 10.1109/IROS.2005.1545153.

[17] D. Fontanelli, F. Shamsfakhr, D. Macii, and L. Palopoli, "An uncertainty-driven and observability-based state estimator for nonholonomic robots," *IEEE Trans. Instrum. Meas.*, vol. 70, pp. 1–12, 2021, doi: 10.1109/TIM.2021.3053066.

[18] J. Solá, "Quaternion kinematics for the error-state Kalman filter," 2017, *arXiv:1711.02508*.

[19] R. Hermann and A. J. Krener, "Nonlinear controllability and observability," *IEEE Trans. Autom. Control*, vol. AC-22, no. 5, pp. 728–740, Oct. 1977, doi: 10.1109/TAC.1977.1101601.

[20] Q. Shi, X. Cui, S. Zhao, J. Wen, and M. Lu, "Range-only collaborative localization for ground vehicles," in *Proc. 32nd Int. Tech. Meeting Satell. Division Inst. Navigat. (ION GNSS)*, Oct. 2019, pp. 2063–2077, doi: 10.33012/2019.16886.

[21] J. Tiemann, O. Fuhr, and C. Wietfeld, "CELIDON: Supporting first responders through 3D AOA-based UWB ad-hoc localization," in *Proc. 16th Int. Conf. Wireless Mobile Comput., Netw. Commun. (WiMob)*, 2020, pp. 20–25.

[22] Y.-H. Cheng, Q.-H. Meng, Y.-J. Liu, M. Zeng, L. Xue, and S.-G. Ma, "Fusing sound and dead reckoning for multi-robot cooperative localization," in *Proc. 12th World Congr. Intell. Control Autom. (WCICA)*, Jun. 2016, pp. 1474–1478, doi: 10.1109/WCICA.2016.7578703.

[23] J. R. Foerster, "The effects of multipath interference on the performance of UWB systems in an indoor wireless channel," in *Proc. IEEE VTS 53rd Veh. Technol. Conf.*, May 2001, vol. 2, no. 53, pp. 1176–1180, doi: 10.1109/VETECS.2001.944566.

[24] R. De Maesschalck, D. Jouan-Rimbaud, and D. L. Massart, "The Mahalanobis distance," *Chemom. Intell. Lab. Syst.*, vol. 50, no. 1, pp. 1–18, 2000, doi: 10.1016/S0169-7439(99)00047-7.

[25] A. Goudar and A. P. Schoellig, "Online spatio-temporal calibration of tightly-coupled ultrawideband-aided inertial localization," 2021, *arXiv:2108.00133*.

[26] J. Sturm, N. Engelhard, F. Endres, W. Burgard, and D. Cremers, "A benchmark for the evaluation of RGB-D SLAM systems," in *Proc. IEEE/RSJ Int. Conf. Intell. Robots Syst.*, Oct. 2012, pp. 573–580, doi: 10.1109/IROS.2012.6385773.

[27] D. Q. Huynh, "Metrics for 3D rotations: Comparison and analysis," *J. Math. Imag. Vis.*, vol. 35, no. 2, pp. 155–164, 2009, doi: 10.1007/s10851-009-0161-2.

[28] InvenSense. (Jun. 20, 2016). *MPU-9250 Product Specification Revision 1.1*. [Online]. Available: https://invensense.tdk.com/wp-content/uploads/2015/02/PS-MPU-9250A-01-v1.1.pdf

[29] Nooploop. (Aug. 11, 2020). *LinkTrack_AOA_Datasheet_V1.1*. [Online]. Available: https://ftp.nooploop.com/software/products/uwb/doc/LinkTrack_AOA_Datasheet_V1.1_zh.pdf

Boli Zhou received the B.S. degree in mechanical engineering from the South China University of Technology, Guangzhou, China, in 2020. He is currently pursuing the M.S. degree in engineering mechanics with the Institute of AI and Robotics, Fudan University, Shanghai, China.

His research interests include robotics, simultaneous localization and mapping, and computer vision.

Hongbin Fang (Member, IEEE) received the B.E. degree in engineering mechanics and the Ph.D. degree in mechanics from Tongji University, Shanghai, China, in 2008 and 2015, respectively.

During 2012 and 2014, he was a joint Ph.D. student in mechanical engineering at the University of Michigan, Ann Arbor, MI, USA. From 2015 to 2017, he was a Postdoctoral Research Fellow with the Department of Mechanical Engineering, University of Michigan. In 2017, he joined The Hong Kong Polytechnic University, Hong Kong, China, where he was a Postdoctoral Research Associate with the Department of Mechanical Engineering. He is currently an Associate Professor (Young Researcher) with the Institute of AI and Robotics, Academy of Engineering and Technology, Fudan University, Shanghai. His research interests include bioinspired robots, locomotion systems, nonlinear dynamics and control, smart materials and structures, origami-based metamaterials, data-driven modeling, and system identification.

Dr. Fang is a member of the American Society of Mechanical Engineers (ASME). He was a recipient of the 2014 SPIE Bioinspiration Best Student Paper Award (First Place).

Jian Xu received the Ph.D. degree in dynamics and control from Tianjin University, Tianjin, China, in 1994.

He is currently a Distinguished Professor and the Director of the Institute on Dynamics and Control, Tongji University, Shanghai, China. He was a Postdoctoral Researcher with the Beijing University of Aeronautics and Astronautics, Beijing, China, from 1994 to 1996, and the Huazhong University of Science and Technology, Wuhan, China, from 1996 to 1998. In 1998, he joined Tongji University as an Associate Professor, where he has been a Professor since 2000. His primary areas of research include locomotion robotics, time-delay induced dynamics, nonlinear dynamics and control, vibration controls, stability, bifurcation and chaos in nature and engineering systems, neural networks with delayed connection, and biological systems.